UiO-66/TiO2 nanostructures as adsorbent/photocatalytic composites for air treatment towards dry dimethyl methylphosphonate-laden air flow as a Chemical Warfare Agent analog

Nina Rouvière, Jean-Philippe Brach, Tom Honnecker, Konstantinos Christoforidis, Didier Robert, Valérie Keller

UiO-66/TiO_2 nanostructures as adsorbent/photocatalytic composites for air treatment towards dry dimethyl methylphosphonate-laden air flow as a Chemical Warfare Agent analog

Nina Rouvière[1], Jean-Philippe Brach[1], Tom Honnecker[1], Konstantinos Christoforidis[1,2], Didier Robert[1], Valérie Keller[1*]

* Corresponding author: vkeller@unistra.fr

1 ICPEES, Institute of Chemistry and Processes for Energy, Environment and Health, UMR 7515 CNRS/University of Strasbourg, 25 rue Becquerel 67087 Strasbourg Cedex 2, FRANCE

2 Department of Environmental Engineering, Democritus University of Thrace, Xanthi 67100, Greece

Abstract

The coupling of UiO-66 to TiO_2 nanoparticles (P25 NP) and nanosheets (NS) at various UiO-66/ TiO_2 ratios was achieved. The obtained composites exhibited high specific area, thus enhancing their DMMP-adsorption capacities. In the case of P25-based composites, the presence of UiO-66 slightly lowered the band gap energy of TiO_2. The total amount of removed DMMP and the breakthrough time were considered as criteria to assess and compare the performance of all materials towards DMMP-laden (330 ppm) flow photodecontamination over 16 h. P25-based composites presented all enhanced decontamination activity considering the total amount of eliminated DMMP compared to bare P25, highlighting the best performance over 10 wt% UiO-66/P25 (92 ± 13 % of total amount of DMMP decontaminated) photocatalyst. On this composite, DMMP was converted into strongly adsorbed MMP, MP and MeOH. DMMP-decontamination performance of NS-based composites remained lower than the P25-based one.

Keywords

Chemical Warfare Agents ; DMMP ; Photocatalysis ; Decontamination ; UiO-66 ; TiO_2

1 Introduction

Despite their prohibition, chemical warfare agents (CWA) are still used in terrorist attacks [1–3] or in conflicts such as in Syria [4–6]. Amongst them, nerve agents are fluorine- or cyanide-organophosphorus compounds (OPCs) exhibiting the lowest lethal threshold [7,8]. In order to protect military or civilian population from exposure, development of rapid broad-range air OPCs removal processes become a crucial issue. The most currently used air OPCs removal process are filters containing adsorbents such as impregnated activated carbon [9,10]. Nevertheless, their decontamination activity remains limited, resulting mostly in the storage of contaminated species and potential desorption/reemission on term [10]. Other alternatives processes were studied for OPCs removal: incineration [10,11], pyrolysis

[11–13], plasma [14,15], and advanced oxidative processes [11]. Among the latter, heterogeneous photocatalysis proved its decontamination ability over a broad range of toxic compounds [16–18]. Titanium dioxide remains the most encountered photocatalyst due to its low cost, non-toxicity, long durability, and thermal and chemical stabilities [19]. Previous studies have already shown its effectiveness towards nerve agents removal [20–26]. However, it has been identified that its charge carrier recombination, low adsorption capacities of some organic pollutants and poisoning, limit its photocatalytic activity for large scale flowing air decontamination.

In recent years, zirconium-base MOFs constitute a promising class of adsorbents for chemical protection filters, which offers high thermal, chemical and mechanical stabilities, tunability, and exceptional specific surface area [27–31]. Among them, UiO-66 demonstrates promising adsorption and decontamination abilities towards OPCs [29,31–35]. Its structure, composed by multiple Zr-OH-Zr moieties, can adsorb and induce catalytic hydrolysis of nerve-agent, reminiscent of the Lewis-acidic Zn-OH-Zn sites found in G-agent destroying phosphotriesterase enzyme [32]. However, the slow kinetics of their nerve agent destruction remains unacceptable for their deployment to protection equipment [29]. In recent years some studies proved synergistic effects between UiO-66 and TiO_2, enhancing their photodegradation abilities towards organic pollutants [36–40]. Crake et al. reported a charge transfer process between UiO-66 and TiO_2 under visible light, hindering electron-hole recombination process [40].

This study focuses on the influence of different TiO_2 morphologies at the nanoscale carried out by comparison of photocatalytic performance of zero-dimensional nanoparticles (NP) and two-dimensional nanosheets (NS) aiming at achieving high surface-to-volume ratio, high photon utilization efficiency and short charge carrier diffusion distances [17,36,41]. The coupling of UiO-66 to these nanostructures was studied as well. Dimethyl methylphosphonate (DMMP) is used as an analog to mimic Sarin for decontamination issues, both of them exhibiting similar oxidized intermediate structures [42], adsorption, transport and vapor-liquid equilibrium properties [43,44]. The photocatalytic performances of UiO-66/TiO_2 composite materials were evaluated towards the decontamination of a dry DMMP-laden air flow, in order to shunt the hydrolysis capacities of UiO-66.

2 Experimental

2.1 *Catalysts synthesis*

All chemical products were used without further purification. TiO_2 P25 powder was purchased from Degussa-Evonik, sodium hydroxide (NaOH, 99%) was purchased from Carlo Erba Reactif, zirconium (IV) chloride ($ZrCl_4$, 99.5 %), terephthalic acid (H_2BDC, 98 %), hydrochloric acid (HCl, 37 %) were purchased from Sigma-Aldrich. N,N-Dimethylformamide (DMF, 99.5 %) was purchased from Fischer Scientific. Dimethyl methylphosphonate (DMMP, 97%) was purchased from Alfa Aesar.

Synthesis of TiO_2 nanosheets (NS). TiO_2 NS were prepared through hydrothermal method, based on previous studies carried out by Grandcolas et al., and Wang et al. [45,46]. 1 g of TiO_2 P25 was stirred into 50 mL of 10 M NaOH aqueous solution in PTFE autoclave (Teflon, 84 mL) for 1 h. The mixture was heated at 130 °C for 24 h in a preheated oven, and washed with 500 mL of 1 M HCl aqueous solution, then deionized water was added until the washing solution reached pH 7. The sample was dried in an oven preheated at 100 °C. A post-thermal treatment was applied at 380 °C for 3 h with a heating rate of 10 °C·min^{-1} under static air.

Synthesis of UiO-66. This synthesis is based on the work of Crake et al. [40]. 0.313 g of $ZrCl_4$, 2.5 mL HCl and 12.5 mL DMF were introduced in a beaker and sonicated for 20 min. 0.335 g of H_2BDC and 25 mL of DMF were added. The mixture was sonicated again for 20 min, transferred to a PTFE autoclave (Teflon, 84 mL) and heated at 150 °C for 24 h in a preheated oven under static air. The autoclave was then cooled down for 3 h to ambient temperature without the help of a cooler. The produced powder was filtered and washed with deionized water, acetone and ethanol (250 mL each). The sample was finally dried in a vacuum oven preheated at 120 °C.

Synthesis UiO-66/TiO_2 composites. TiO_2 P25 and TiO_2 NS are labeled as P25 and NS, respectively. P25 or NS were mixed with different amounts of UiO-66 reaching x wt% (nominal) in the final composite (x = 10, 15, 30 wt%). The resulting nanocomposites are labeled x wt% UiO-66/P25 or NS, referring to their respective compositions. Firstly, TiO_2 powders and UiO-66 were mixed together in a mixture of 20 mL of deionized water and 30 mL of ethanol for 1 h. The mixture was sonicated for 15 min, then dried at 100 °C in an oven preheated during 18 h. The obtained powder was grinded in a mortar, then calcined at 200 °C for 3 h (5°C.min^{-1} heating ramp) under static air. For comparison, bare UiO-66, P25 and NS were annealed at the same calcination temperature and named as annealed precursors.

2.2 *Characterization methods and photocatalytic assessment*

High Resolution Transmission Electron Microscopy (HRTEM) and Transmission Electron Microscopy (TEM) were performed on a Jeol 2100F equipped with lanthanum hexaboride cathode alimented by a 200 kV tension. FFT transformation were calculated from HRTEM images with ImageJ software.

X-ray diffraction (XRD) measurements were performed using a Bruker D8 Advance apparatus, equipped with a Lynxeye XE detector operating at 40 kV and 40 mA in θ/2θ mode. The source of the X-Rays is a copper anticathode (Kα = 1.5418 Å). Acquisition was performed in 2θ scanning mode on the 5-90° range with steps of 0.026°. The mean crystal thickness is calculated from the Debye-Scherrer equation based on the full width at half maximum and the position of the most intense peaks at 2θ values of 7,4°, 25,3° and 27,5° corresponding to UiO-66, TiO_2 anatase and rutile crystals respectively.
Thermogravimetric analyses (TGA) were processed on a TA Instrument Q 5000 IR apparatus equipped with a sample changer and a microbalance with a sensitivity of around 0.1 µg. 3

mg of each sample were placed in a platinum crucible and heated from 50°C to 760°C. TGA performed on all samples before the DMMP-photodecontamination, the temperature ramp was 10 °C.min^{-1} under static air. As the synthesis process should preserve the properties of each counterpart, UiO-66 content in UiO-66/TiO_2 composites can be calculated as followed:

$$UiO-66\ content\ (\%wt) = \left[\frac{Composite\ weight\ loss\ -\ Annealed\ TiO_2 weight\ loss}{Annealed\ UiO-66\ weight\ loss\ -\ Annealed\ TiO_2 weight\ loss}\right]\cdot 100$$

TGA performed on 10 wt% UiO-66/P25 after DMMP-photodecontamination used a temperature ramp of 25°C.min^{-1} under a N_2 flow of 50 cm^3.min^{-1}.

Temperature Programmed Desorption (TPD) were performed on a Micromiritics Autochem II coupled to a Pfeiffer Thermostar mass spectrometer. 50 mg of each samples were heated from 50°C to 760°C, with a temperature ramp of 25°C.min^{-1} under a N_2 flow of 50 cm^3.min^{-1}.

Nitrogen adsorption and desorption isotherms were performed using a Micromeritics ASAP 2420 sorption analyzer. Prior to the analysis, the samples were preheated at 150°C (temperature ramp of 10°C.min^{-1}) for 5h for outgassing. The analysis was carried out under atmospheric pressure at -196°C. The surface areas were calculated from the Brunauer-Emmet-Teller (BET) method. As previously assumed, UiO-66 content in UiO-66/TiO_2 composites can be calculated as followed:

$UiO-66\ content\ (\%wt) = \left[\frac{Composite\ S_{BET} - Annealed\ TiO_2 S_{BET}}{Annealed\ UiO-66\ S_{BET} - Annealed\ TiO_2 S_{BET}}\right]\cdot 100$, where S_{BET} is the surface area (m².g^{-1}) calculated by BET. Pores distributions were calculated from Barrett-Joyner-Halinda method according to desorption values over a range of pores of 1.9 nm and 300 nm diameter.

UV-visible absorption spectra were recorded in solid state on a Perkin Elmer 950 spectrophotometer fitted with a Labsphere RSA ASSY 100 nm integrating sphere. The spectra were acquired in reflection mode over a range of 200-800 nm. In order to determine the absorbance coefficient, the diffuse reflectance spectra were converted to Kubelka-Munk units via the equation: $F(R) = \frac{(1-R)^2}{2R}$. To obtain the band gap energy (Eg) of the semiconductor, the Tauc equation $(F(R)^{*}h\nu)^{S} = (h\nu - Eg)$ was used where h is the Planck constant, v is the frequency and S = ½ and 2 as respective coefficients for TiO_2 and UiO-66, as they are respectively considered as indirect and direct semiconductors.

Photoluminescence (PL) spectra were analyzed in solid state on a Horiba S2 Jobin Yvon Fluoromax-4 spectrofluorometer over a range of 420-600 nm. Samples were excited at 368 nm. A filter for wavelength lower than 395 nm was introduced in the spectrofluorometer in order to shunt the photolumiunescence caused by the UV-absorbance of the self-emission light of materials. All PL spectra were corrected.

Attenuated Total Reflectance Fourier Transform Infrared (ATR-FTIR) spectra were recorded on a Thermo Fischer Nicolet 380 FT-IR with Smart Orbit Diamond in solid state in absorbance mode, over the wavenumber range from 400 to 4000 cm^{-1}.

Gas-phase DMMP photodecontaminations were carried out in a 350 mm length and 320 mm outer diameter tubular Pyrex reactor. The inner diameter of 280 mm was coated by 200 mg

of photocatalyst on 300 mm of length according to the process shared in the Supporting Information (Fig.S1). DMMP vapors were generated upstream by bubbling air through liquid DMMP, contained into a thermo-controlled saturator. These vapors were then diluted with a dry air flow to obtain a continuous 330 ppm DMMP-laden flow of 200 $cm^3.min^{-1}$ over 16 h. Outgoing flows from the reactor were analyzed by an Agilent GC-6890N Gas Chromatography coupled to an Agilent MS-5973N mass spectrometer. For all experiments, with a standard deviation of the GC/MS analyses of 13 %. The column (Agilent HP-5MS 30 m x 0.250 mm) was hold during 4 min at 40°C, then heated to 110°C with a rate of 25°C/min. Helium was used as carrier gas. DMMP photodecontamination was investigated in the dark and under UV, where photocatalysts were activated by a UV-A Sylvania F8W T5 BL368 tubular lamp providing 22.75 kW/m² total UV-A irradiance (315-400 nm). The lamp possessed a spectral peak centered around 368 nm (Fig.S1), and was inserted into the tubular reactor, protected by a quartz tube from toxic gases.

3 Results and discussion

3.1 *Structural properties*

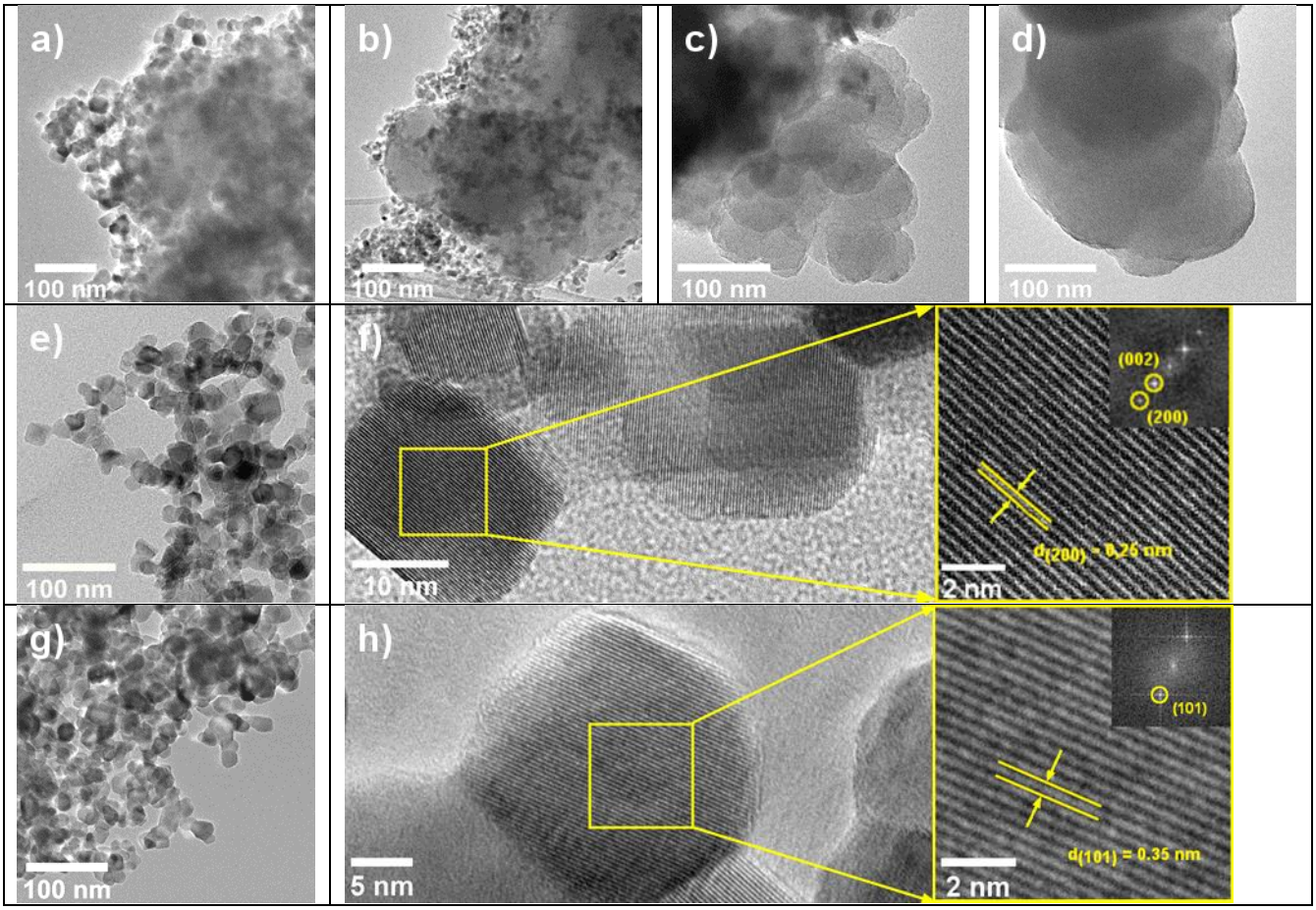

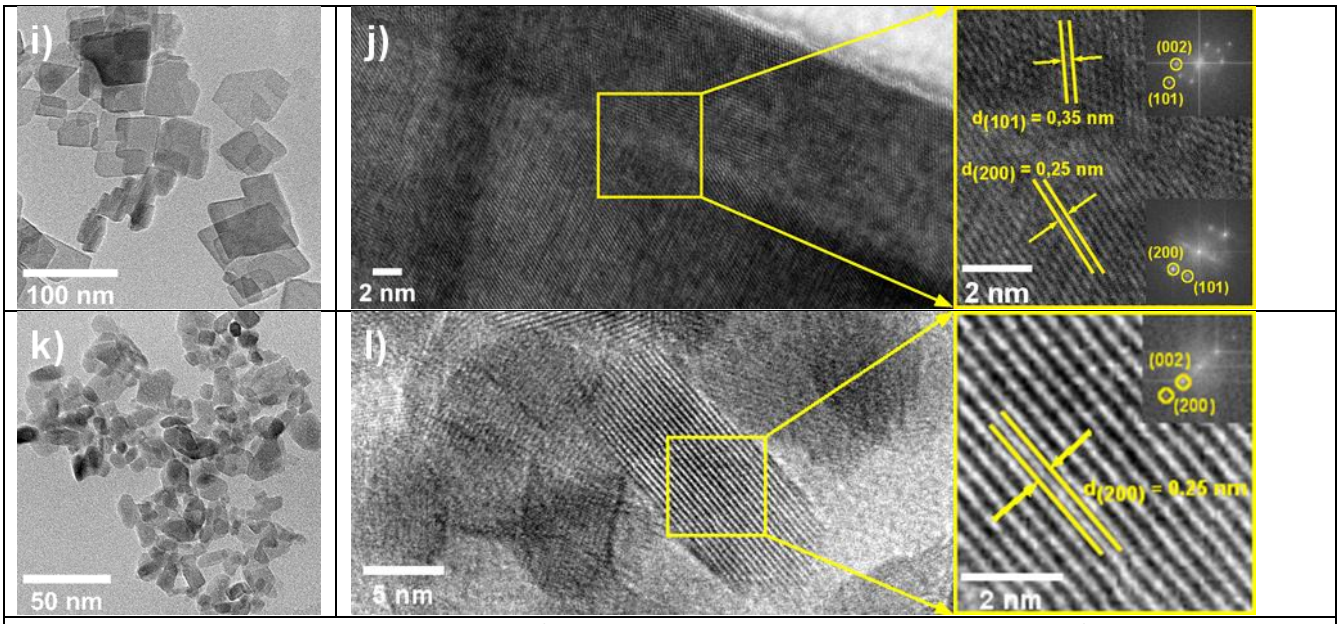

Fig.1: TEM, HRTEM and FFT images of UiO-66/TiO_2 and their counterparts: (a) 10 wt% UiO-66/P25, (b) 10 wt% UiO-66/NS composites, (c) bare UiO-66, (d) annealed UiO-66, (e) and (f) bare P25, (g) and (h) annealed P25, (i) and (j) bare NS, (k) and (l) annealed NS.

According to TEM analysis (Fig.1.c,d), unshaped particles of bare and annealed UiO-66 were observed, due to their organic amorphous BDC linker. After annealing, the particle size of UiO-66 increased from an average diameter of 61 nm to 240 nm. An average diameter of 21 nm was measured for bare and annealed commercial anatase P25 nanoparticles (Fig.1.e,f,g,h). TEM images evidenced the formation of NS morphology (Fig.1.i). Their lateral surface corresponded to anatase crystal plane (200) [47], while their thickness of 7 nm showed the lattice spacing of (101) plane (Fig.1.j). Because of their polymorphology, the length of the NS could not be measured. Annealing of NS led to their fragmentation into smaller NS (Fig.1.k), while preserving their anatase crystal structure and thickness (Fig.1.l). One can observe the conservation of structures of the annealed counterparts in the composites (Fig.1.a,b), where UiO-66 particles were deposited on P25 and NS particles.

P25 is a well-known mixture of TiO_2 anatase and rutile crystalline phases [48]. Although NS were synthetized from P25, the rutile phase was no more evidenced (Fig.2.b). XRD pattern proved the achievement of UiO-66 crystallization [28,40]. Post-thermal treatment did not affect the crystallinity of TiO_2 references, however, it favored the growth of UiO-66 crystallites whose thickness increased from 21 nm to 38 nm (Table S1). UiO-66/P25 and UiO-66/NS composites exhibited the same diffraction peaks and crystallite thickness as their respective annealed TiO_2 and UiO-66 counterparts, providing evidence that their structures were not altered by the synthesis process and that no new structured appeared.

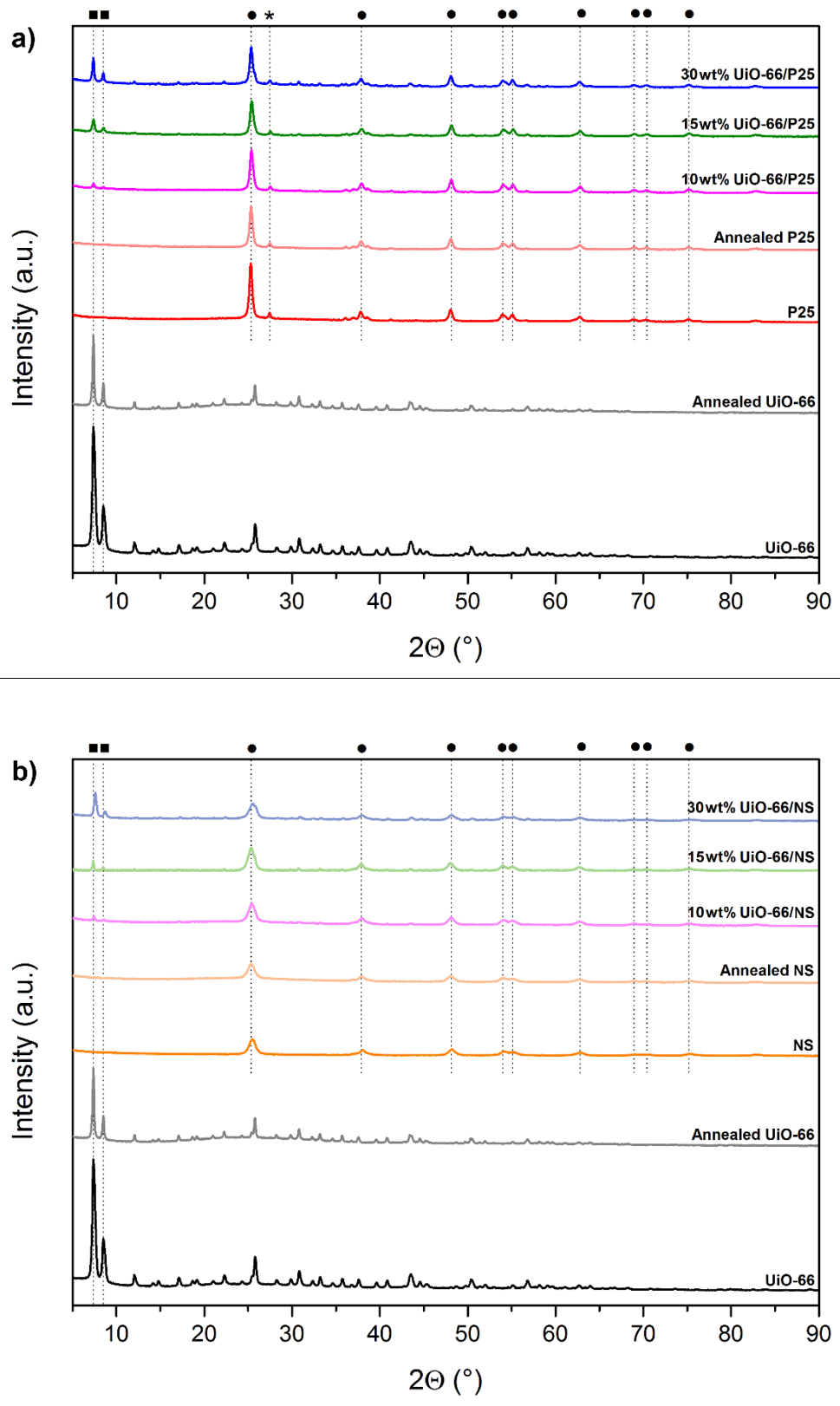

*Fig.2: XRD pattern of (a) UiO-66/P25 and (b) UiO-66/NS composites compared to bare and annealed TiO_2 and UiO-66 counterparts: ▪ UiO-66, • TiO_2 anatase and * rutile phase.*

3.2 *Determination of UiO-66 content*

Bare P25 and NS exhibited a total weight loss of *ca.* 3 and 4 % at 760°C (Table 1), corresponding mainly to water desorption and surface hydroxyl groups elimination or restructuration, meanwhile their annealed counterparts lose respectively *ca.* 3 and 5 % of relative weight. Annealing of TiO_2 nanostructures did not cause any further degradation. From TGA curves of the reference UiO-66 (Fig.S4), three weight losses were observed: below 100°C (physical adsorbed water or the residual chemicals), between 80°C-250°C (dehydratation of $Zr_6O_4(OH)_4$ nodes into Zr_6O_6) and at 470°C (decomposition of BDC linkers) [28,49]. Annealed UiO-66 differed from its bare counterpart by a lower weight loss below 100°C, assigned to water or chemicals residuals. Composites showed the same relative weight losses as their counterparts.

N_2 adsorption-desorption isotherms (Fig.S5) presented UiO-66 as a microporous material exhibiting high surface area of *ca.* 1022 $m^2.g^{-1}$. P25 and NS are mesoporous materials, of *ca.* 64 $m^2.g^{-1}$ and 151 $m^2.g^{-1}$ of surface area respectively. NS morphology increased TiO_2 surface area, thus due to enhancement of the large surface-to-volume ratio [45]. The post-thermal treatment did not affect TiO_2 surface behavior. Nevertheless, UiO-66 was impacted by this treatment, resulting in the decrease of its surface area from *ca.* 1022 m^2/g to 931 m^2/g. As meso- and macropores distribution (Fig.S6) did not show any difference between bare and annealed UiO-66, it is supposed that annealing of UiO-66 impacted its microporosity, thus resulting in the growth of MOF crystallites. Coupling TiO_2 with UiO-66 increased microporosity in the UiO-66/TiO_2 composites. Loss of mesopores of NS centered at 12 nm of diameter was linked to the increase of UiO-66 content for NS-based composites. Pores population of P25 centered at 2 nm of diameter disappeared from porous distribution of P25-based composites, whereas a new pore population centered at 34 nm was observed, due to the aggregation of P25 particles.

Table 1 summarizes weight losses at 760°C deduced from TGA analyses and surface areas calculated from BET analysis for UiO-66/TiO_2 composites and their counterparts. Experimental UiO-66 content in composites were deduced from these data. Considering experimental errors, UiO-66 experimental content remained close to the theoretical ones expected. It confirms the absence of modifications of TiO_2 and UiO-66 structures during elaboration of the composites.

Table 1: Determination of UiO-66 content and band gap energy from TGA, BET and UV-Visible absorption analysis of UiO-66, P25, NS, and UiO-66/TiO_2 composites.

Sample	TGA		BET		Band gap energy (eV)
	Experimental relative weight loss (%)	Experimental UiO-66 content (wt%)	Experimental surface area ($m^2.g^{-1}$)	Experimental UiO-66 content (wt%)	
UiO-66	59 ± 1	-	1022 ± 10	-	4.01
Annealed UiO-66	57 ± 1	-	931 ± 9	-	4.35
P25	3 ± 0	-	64 ± 0	-	3.23

Annealed P25	3 ± 0	-	65 ± 0	-	3.19
NS	4 ± 0	-	151 ± 2	-	3.17
Annealed NS	5 ± 0	-	156 ± 2	-	3.25
10wt% UiO-66/P25	7 ± 0	7.5	136 ± 1	8.0	3.11
15wt% UiO-66/P25	9 ± 0	11.0	167 ± 2	12.0	3.11
30wt% UiO-66/P25	17 ± 0	26.0	318 ± 3	29.0	3.19
10wt% UiO-66/NS	9 ± 0	7.0	228 ± 2	9.5	3.19
15wt% UiO-66/NS	17 ± 0	15.0	240 ± 2	13.5	3.20
30wt% UiO-66/NS	23 ± 0	34.0	370 ± 4	28.5	3.25

3.3 *Photoelectronic properties*

Bare and annealed UiO-66 harvested UV-A light from 200 nm to a shoulder peak extending the absorption to 336 nm (Fig.3). Two UV-absorption bands were located at 270 nm and 288 nm. Previous works identified the former as absorption of Zr–O oxoclusters [50,51] and the second one to the linker-based absorption influenced by the nearby metal centers [51], confirmed by the red shift observed in comparison with H_2BDC UV-absorption spectrum (Fig.S7.a). UV-light absorption spectra of UiO-66 showed also a negative absorption at 334 nm caused by photoluminescence behavior correlated to the linker-to-cluster charge transfer [50,52]. These phenomenon decreased in line with post-thermal treatment [52]. P25 (Fig.S7.b) and NS (Fig.S7.c) absorbed UV-light over all UV spectrum from 200 nm to 400 nm. Post-thermal treatment did not affect these properties for P25, while a blue shift occurred from bare to annealed NS. This shift may be correlated to the fragmentation of the NS observed on TEM analysis (Fig.1), the disappearance of impurities issued from synthesis or to an enhanced crystallization. All band gaps energies determined by UV spectra are reported in Table 1. In semiconducting MOF, such as UiO-66, the valence band (VB) and conduction band (CB) are commonly regarded as the HOMO corresponding to the energy level of the organic linker, and LUMO representing the redox potential of the metal-oxo-cluster, respectively [53]. Literature reported UiO-66 as a n-type semiconductor characterized by a LUMO potential of BDC linker at -0.6 V vs. NHE (at pH = 7) [53]. Both P25 and anatase NS were reported as n-type semiconductor, of CB calculated to be -0.27 V and -0.22 V vs. NHE (pH = 7) respectively [54,55]. Considering the following equation: $\mathrm{E_g} = \mathrm{E_{CB}} - \mathrm{E_{VB}}$, E_{VB} of UiO-66, P25 and NS should correspond to 3.41 V, 2.96 V and 2.95 V respectively.

UiO-66/P25 composites conserved P25 UV-light absorption properties, whereas the width of UV-light absorption of UiO-66/NS decreased with the increase of UiO-66 content, shifting their peaks maxima from 360 nm for 10 wt% UiO-66/NS to 340 nm for 30 wt% UiO-66/NS. However, the band gap energy of TiO_2 (Table 1) determined from Tauc Plot were estimated to be 3.11 eV for 10 wt% and 15 wt% UiO-66/P25 which is lower than the one determined on bare and annealed P25 (3.19 eV). Meanwhile, the corresponding band gap of NS-based composites was not modified.

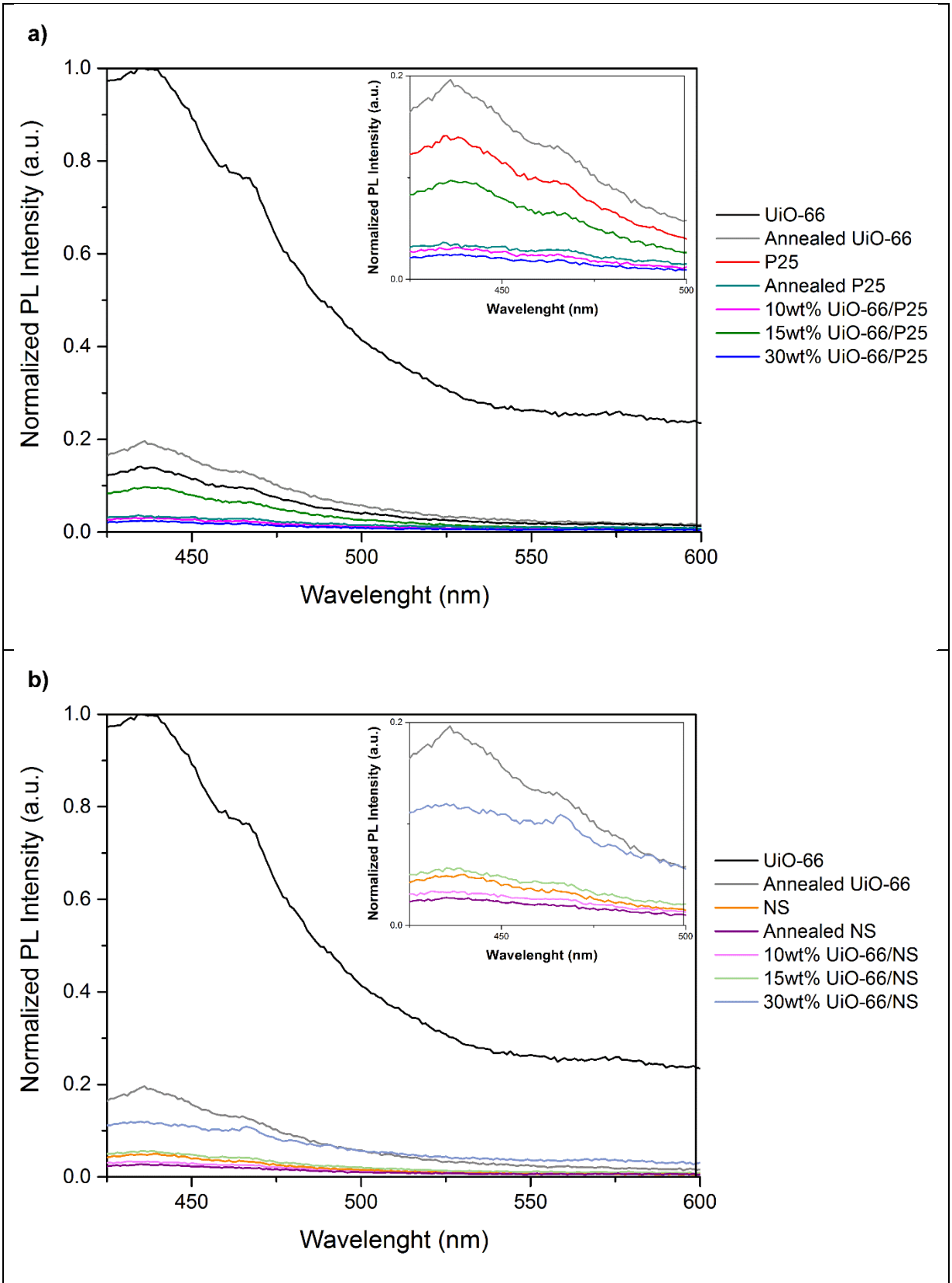

Fig.3: PL properties measurement of: (a) UiO-66/P25 and (b) UiO-66/NS composites, compared to bare and annealed TiO_2 and UiO-66 counterparts, excited at 368 nm.

Bare UiO-66, P25 and NS PL properties were higher than their respective annealed counterparts (Fig.3), due to a size modification of particles or a lower presence of defects by pursuing the crystallization through the thermal treatment [50,52]. In the case of TiO_2 materials, PL properties are suggested to be originated from radiative recombination of self-trapped charges carriers [56]. The respective intensities of their PL behavior were ordered as followed: Annealed NS > Annealed P25 > NS > P25. It can be concluded that annealing process and nanostructuration into nanosheets enhanced the charge separation. Annealed NS are suspected to possess the highest photon utilization efficiency.

As a heterojunction, PL properties of UiO-66/TiO_2 composites should be decreased, compared to the ones of their TiO_2 counterparts. For P25-based composites, 10 wt% and 30 wt% UiO-66/P25 showed lowered PL intensities than annealed P25, confirming the best charge separation (Fig.3.a). All NS-based composites, however, recorded PL intensities higher than annealed NS (Fig.3b). Even bare NS presented less recombination than 15 wt% and 30 wt% UiO-66/NS. Is it suspected that heterojunction between UiO-66/NS was less effective towards photon utilization efficiency than the nanostructuration alone, due to the introduction of defects at the UiO-66/TiO_2 interfaces which acted as recombination centers [57].

3.4 *DMMP photodecontamination*

Fig.4 presents the photocatalysts efficiencies towards DMMP abatement carried out during 16 h on a continuous contaminated dry flow, exported from the abatement curve illustrated on Fig.S8. The photoexcitation under UV light of TiO_2 materials and UiO-66/TiO_2 composites doubled the conversions of DMMP than in the dark, where DMMP supposedly only adsorbed on the materials surfaces. Bare and annealed UiO-66 however were more efficient in dark conditions, due to their faster surface poisoning during the photocatalysis by by-products. This phenomenon also explains the best breakthrough time obtained for P25, NS and 15 wt% UiO-66/P25 without UV light. Bare UiO-66 recorded the highest breakthrough time (303 min) while decontaminating 64 ± 8 % of DMMP generated during 16 h, due to its high specific area. However, the breakthrough time decreased to 185 min after the annealing of UiO-66, probably caused by the growth of UiO-66 crystallites resulting in decreased surface-to-volume ratio and thus the access to the active adsorbent Zr-OH-Zr moieties. Compared to bare TiO_2 nanostructures, annealed P25 and NS exhibited higher breakthrough time, of 133 min and 221 min, respectively. Previous works showed enhancement in photocatalytic activity of TiO_2 by a simple thermal treatment in air due to a higher density of surface oxygen species or to the achievement of better crystallization [58,59]. Bare and annealed NS recorded both higher breakthrough times and total amount of removed DMMP during 16 h than their P25 counterparts. These abilities may be due to the higher specific area which impacts positively adsorption of DMMP, or the enhancement of spatial charge separation proved earlier by PL investigations.

Coupling TiO_2 to adsorbents may provide higher concentrated environment of target compounds surrounding the photocatalytic sites, thus favoring their conversion [60].

Nevertheless, at too large adsorbent contents, the relative increase in density of adsorption sites compared to the photocatalytic ones may become unfavorable for photocatalysis, thus also hindering adsorbent regeneration, which limits adsorption capacity and leads to the poisoning of the active photocatalytic sites. In addition, one can also mention that the presence of the adsorbent in close contact with TiO_2 photocatalyst may also increase the diffusion lenght of the target compounds from the adsorbent's sites to the photocatalytic active sites. Consequently, an optimum in photocatalytic/adsorption sites ratio and interface quality appears necessary for an improved photocatalytic removal. Increasing the amount of UiO-66 coupled with P25 decreased the total DMMP removed. The optimum amount of UiO-66 was 10 wt%, allowing decontamination of 92 ± 13 % of the total DMMP generated over 16 h with a breakthrough time of 112 min. This composite exhibited an enhancement of the DMMP-photodecontamination due to a higher specific area and a better charges separation compared to annealed P25, and showed the highest decontamination efficiency among all the evaluated materials. 30 wt% UiO-66/P25 presented a higher breakthrough time than 15 wt% UiO-66/P25 (respectively 18 and 76 min), meanwhile its photodecontamination activity remained lower. It can be considered that 30 wt% UiO-66/P25 possessed higher adsorption capacities than photocatalytic ones, limiting its photocatalytic activity.

The breakthrough time measured with 15 wt% UiO-66/NS was the highest recorded within this series of materials (243 min), which outperformed the annealed NS one. This difference can be assigned to its higher surface area, which ensures a better DMMP adsorption and decontamination. This high photocatalytic activity yielded however to a larger surface poisoning due to higher intermediates phosphates production and thus deactivation (Fig.S8.c). The post-breakthrough time stabilization of this material showed an abatement of 130 ppm, meanwhile 10 wt% UiO-66/NS decontaminated over 180 ppm, thus explaining their similar DMMP-decontamination capacities (61 ± 8 %) over 16 h. As for the P25-based composites, introducing 30 wt% of UiO-66 into NS-based composite certainly led to higher adsorption capacities than photocatalytic ones (Fig.4.c).

NS 2D morphology is preferred to achieve high quality interface [17,36,41], nevertheless the DMMP-photodecontamination capacities of bare and annealed NS were unexpectedly higher than the ones of NS-based composites. P25-based composites presented all higher total amount of decontaminated DMMP over 16 h than NS-based ones, due to higher charge recombination occuring at UiO-66/NS interfaces. Moreover, theses interfaces may also limit the access to photocatalytic sites, probably due to obstruction of the porosity by UiO-66 favorized by the flat and small size of NS particles.

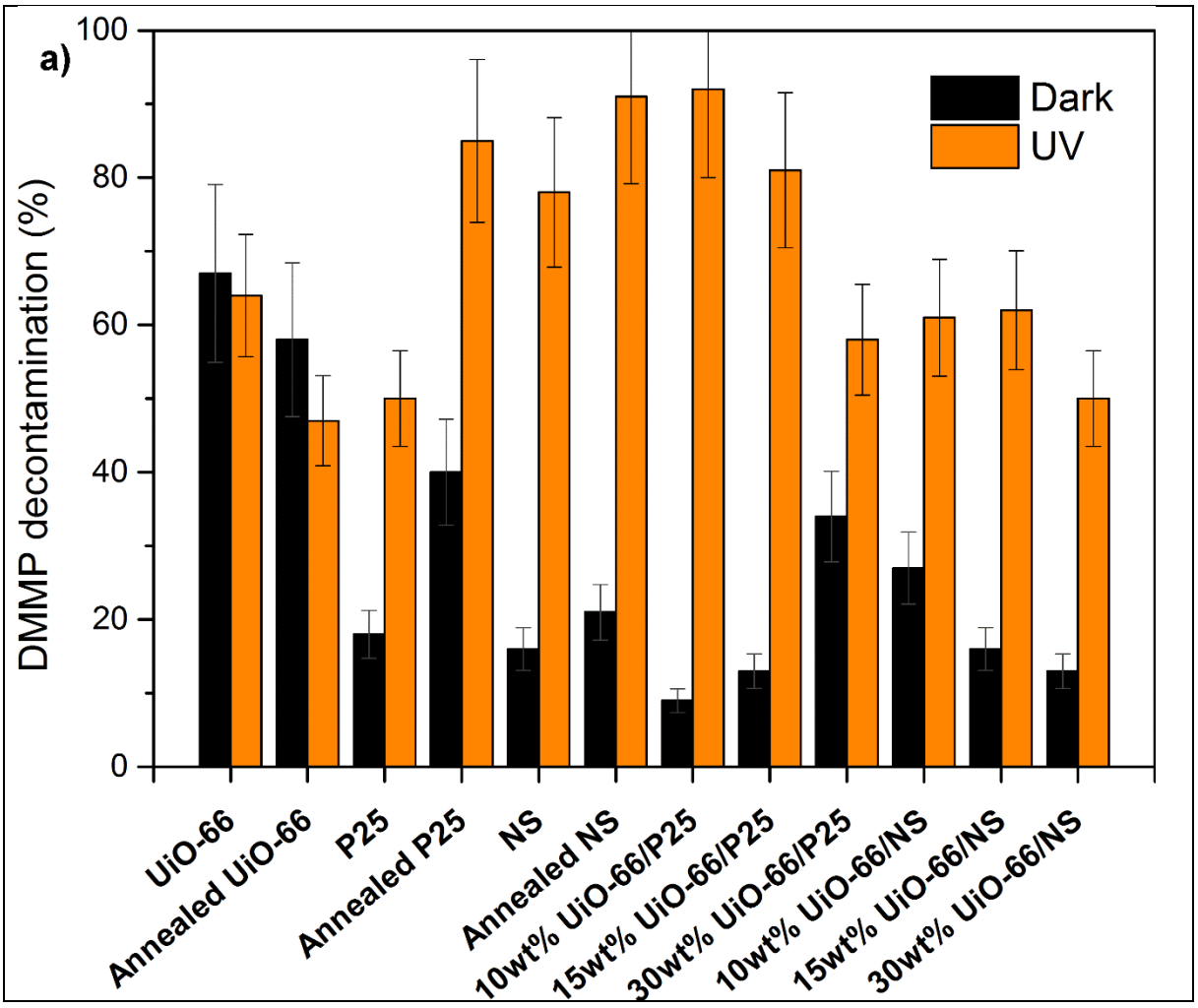
a)
DMMP decontamination (%)
100
80
60
40
20
0
Dark
UV
UiO-66
Annealed UiO-66
P25
Annealed P25
NS
Annealed NS
10wt% UiO-66/P25
15wt% UiO-66/P25
30wt% UiO-66/P25
10wt% UiO-66/NS
15wt% UiO-66/NS
30wt% UiO-66/NS

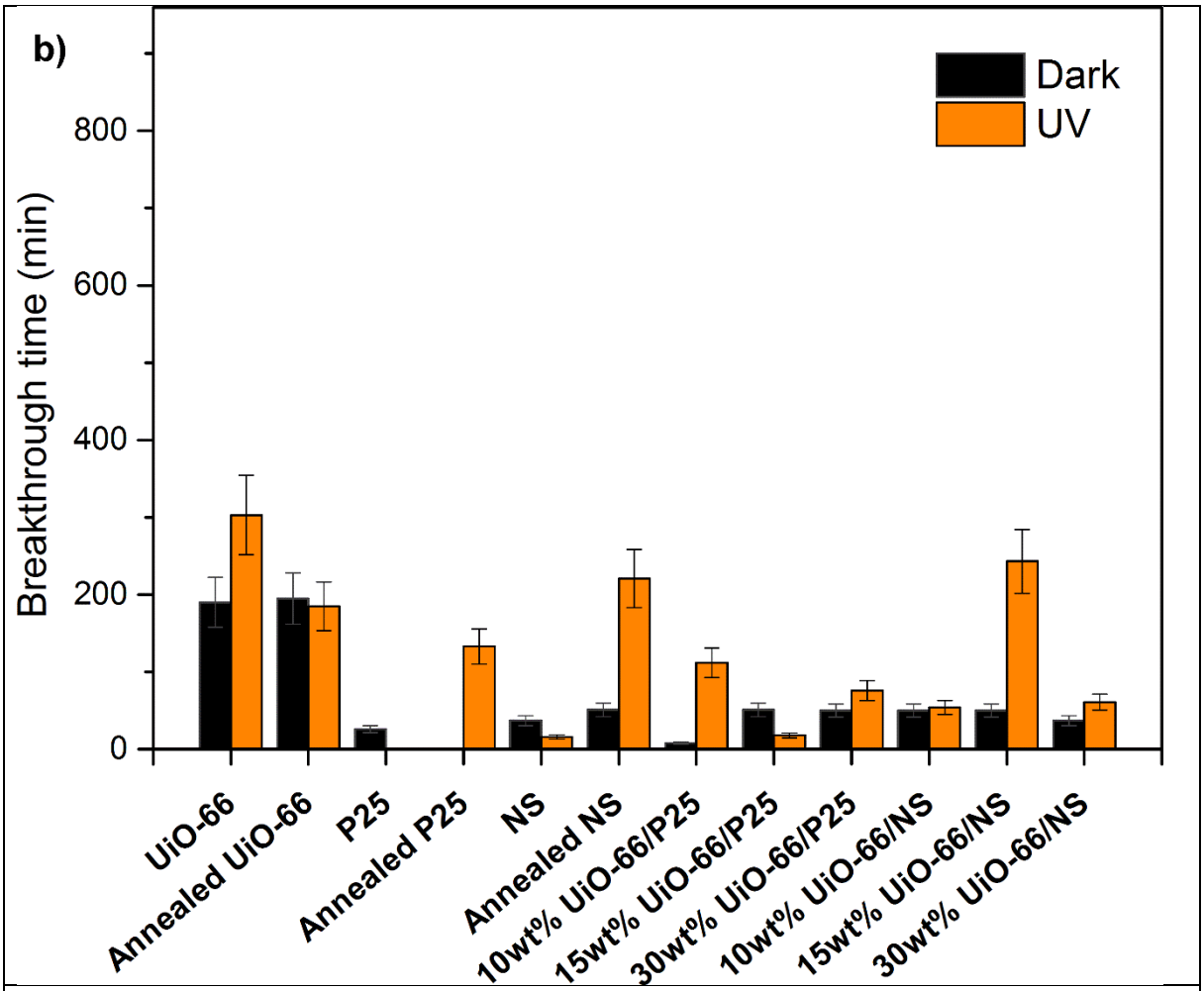

Fig.4: DMMP-photodecontamination capacities of UiO-66/TiO_2 composites compared to TiO_2 and UiO-66 bare and annealed counterparts: (a) total quantity of DMMP decontaminated over 16 h, and (b) breakthrough time.

3.5 *Mechanism and by-products*

No gaseous by-products were recorded during DMMP photodecontamination. Post-DMMP-photodecontamination surface investigations were performed on 10 wt% UiO-66/P25 (Fig.5), as this composite presented the best DMMP-photodecontamination efficiencies. Three main mass losses were identified through TGA (Fig.S9): from 180°C to 230°C (7,07 wt%), and from 230°C to 350°C (7,01 wt%), and BDC linker degradation at 470°C (1,15 wt%). The mass loss from 180°C to 230°C was correlated to the release of species composed by fragments of m/z ratio of 94, 79, 46, 32 and 16 (Fig.S9). DMMP is known to be thermodegraded from 181°C, into the main fragments $[C_2H_7O_2P]^{+\bullet}$ (m/z = 94) and $[CH_4O_2P]^+$ (m/z = 79), with relative abundances of 100 and 78 respectively [61]. As theses abundances were not respected, it suggests the presence of others phosphates species adsorbed on the surface, confirmed by ATR-FTIR spectra (Fig.S10). The release of methanol (m/z = 32) at 230°C, and one of its main products of thermodegradation, dimethyl ester (m/z = 46), may be related to the presence of MMP and or MP adsorbed on the composite's surface. These are well-known DMMP-photodecontamination by-products, obtained through P-O cleavage by h^+ or $^\bullet OH$ species [23,26], which are responsible for IR absorbance band at 1111 cm^{-1} and

1188 cm^{-1} attributed relatively to adsorbed methanol and O-P-O bonds mixed to O-CH_3 [62]. MMP presence is confirmed by the second peak of methanol occurring at 350°C, releasing by the thermoconversion of MMP into MP. At 650°C, a peak of methane (m/z = 16) is associated to the degradation of all organics and oxidation of phosphates species (PO_x species). All of these observations echo the thermodegradation mechanism of DMMP by-products highlighted by Chen et al [63].

The mass loss of 1,75 wt% at 470°C correlated to BDC linkers degradation remained reduced, compared to the one recorded before photodecontamination (3,75 %). Correlations between the shift of O-C-O of BDC linker (Fig.S10) and the disappearance of diffraction peak related to UiO-66 structure after DMMP-photodecontamination (Fig.S11), may confirm the collapsing of UiO-66 structure. However, C=C IR absorbance band related to BDC linkers were unchanged, suggesting that they were not totally photodegraded. This collapsing of the UiO-66 resulted from the P25 photoactivity, as the structure remain intact after the photodegradation of DMMP by UiO-66 photoactived by UV (Fig.S10).

Considering also that photodecontamination was performed in dry atmosphere, and no drop of surface IR hydroxyls was recorded after the photodecontamination (Fig.S10). One may concluded that $^{\bullet}OH$ radicals were not implied into DMMP-photodegradation, and suggests the P-O cleavage by h^+:

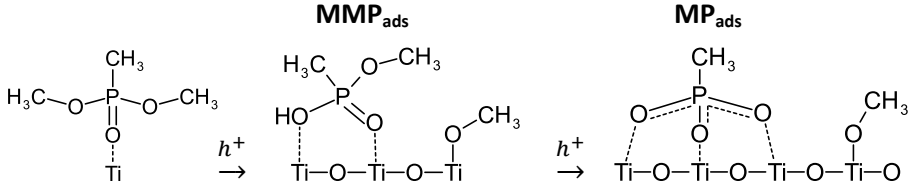

4 Conclusion

Continuous photodecontamination of a 330 ppm DMMP-laden flow was carried out over 16 h on various UiO-66/TiO_2 (NP or NS) compositions, and compared to their counterparts, regarding the total amount of removed DMMP and the breakthrough time as main criteria. Annealing bare TiO_2 NP and NS increased considerably the photocatalytic activity, assuming a higher density of surface oxygen species and/or a better crystallinity. Thermal treatment of UiO-66 resulted in increased crystallites, reducing its surface-to-volume ratio and presumably the access to its adsorption and hydrolysis-inducing Zr-OH-Zr sites. Coupling UiO-66 to TiO_2 only led to enhancement of DMMP removal performance only in the UiO-66/P25 series. The highest DMMP-photodecontamination ability corresponded to 92 ± 13 % of DMMP removal, performed by 10 wt% UiO-66/P25. This composite led to the conversion into MMP, MP, and strongly adsorbed phosphates by P-O cleavage by h^+ onto its surface. One may assume that it results from the best compromise between photon harvesting, charge carrier separation, high DMMP adsorption ability due to optimized UiO-66/TiO_2 interface.

Acknowledgement

This work was partially supported by NBC-Sys and the National Association of Research and Technology (ANRT). Financial support from the French National Research Agency (ANR) under the Program "Make Our Planet Great Again" (ANR-18-MOPGA-0014) is also acknowledged. The author are grateful to Ihiawakrim D. and Ramnarain V. for the TEM analysis.

References

[1] Oppenheimer A., *OPCW* **2008**.
[2] Technical Secretariat, *S/1612/2018*, OPCW, **2018**.
[3] Technical Secretariat, *S/1671/2018*, OPCW, **2018**.
[4] Technical Secretariat, *S/1510/2017*, OPCW, **2017**.
[5] Technical Secretariat, *S/1636/2018*, OPCW, **2018**.
[6] Technical Secretariat, *S/1943/2021*, OPCW, **2021**.
[7] L. Szinicz, *Toxicol* **2005**, *214*, 167-181.
[8] H. Thiermann, F. Worek, K. Kehe, *Chem. Biol. Interact.* **2013**, *206*, 435.
[9] K. Won-In, J. Chaiprapa, P. Chirawatkul, P. Dararutana, *Mater. Sci. Eng.* **2020**, *744*, 1-9.
[10] K. Kim, O. Tsay, D. Atwood, D. Churchill, *Chem. Rev.* **2011**, *111*, 5345-5403.
[11] J. Nawała, P. Jóźwik, S. Popiel, *Int. J. Environ. Sci. Technol.* **2019**, *16*, 3899-3912.
[12] S. Neupane, R. Rahman, J. Baker, F. Arafin, E. Ninnemann, K. Thurmond, C.-H. Wang, A. Masunov, S. Vasu, *Combust. Flame* **2020**, *214*, 14-24.
[13] D. Van Buren, T. Mueller, C. Rosenker, J. Barcase, K. Van Houten, *J. Anal. Appl. Pyrolysis* **2021**, *154*, 105007-105011.
[14] H. Herrmann, G. Selwyn, I. Henins, J. Park, M. Jeffery, J. Williams, *IEEE Trans. Plasma Sci.* **2002**, *30*, 1460-1470.
[15] D. Kim, B. Gweon, S. Moon, W. Choe, *Curr. Appl. Phys.* **2009**, *9*, 1093-1096.
[16] J. Peral, X. Domènech, D. Ollis, *J. Chem. Technol. Biotechnol.* **1997**, *70*, 117-140.
[17] S. Verbruggen, *J. Photochem. Photobiol. C* **2015**, *24*, 64-82.
[18] A. Luengas, A. Barona, C. Hort, G. Gallastegui, V. Platel, A. Elias, *Rev. Environ. Sci. Biotechnol.* **2015**, *14*, 499-522.
[19] A. Mills, S. Le Hunte, *J. Photochem. Photobiol. A* **1997**, *108*, 1-35.
[20] J. Moss, S. Szczepankiewicz, E. Park, M. Hoffmann, *J. Phys. Chem. B* **2005**, *109*, 19779-19785.
[21] N. Mera, T. Hirakawa, T. Sano, K. Takeuchi, H. Ichinose, Y. Seto, N. Negishi, *Appl. Catal. B* **2014**, *146*, 71-78.
[22] T. Hirakawa, K. Sato, A. Komano, S. Kishi, C. Nishimoto, N. Mera, M. Kugishima, T. Sano, H. Ichinose, N. Negishi, Y. Seto, K. Takeuchi, *J. Phys. Chem. C* **2010**, *114*, 2305-2314.
[23] T. Obee, S. Satyapal, *J. Photochem. Photobiol. A* **1998**, *118*, 45-51.
[24] C. Rusu, J. Yates, *J. Phys. Chem. B* **2000**, *104*, 12299-12305.
[25] N. Mera, T. Hirakawa, T. Sano, K. Takeuchi, Y. Seto, N. Negishi, *J. Hazard. Mater.* **2010**, *177*, 274-280.
[26] A. Vorontsov, L. Davydov, E. Reddy, C. Lion, E. Savinov, P. Smirniotis, *New J. Chem.* **2002**, *26*, 732-744.
[27] S. Biswas, P. Van Der Voort, *Eur. J. Inorg. Chem.* **2013**, *2013*, 2154-2160.
[28] M. Kandiah, M. Nilsen, S. Usseglio, S. Jakobsen, U. Olsbye, M. Tilset, C. Larabi, E. Quadrelli, F. Bonino, K. Lillerud, *Chem. Mater.* **2010**, *22*, 6632-6640.

[29] J. DeCoste, G. Peterson, *Chem. Rev.* **2014**, *114*, 5695-5727.
[30] Y. Huang, W. Qin, Z. Li, Y. Li, *Dalton Trans.* **2012**, *41*, 9283-9285.
[31] M. Kalaj, M. Momeni, K. Bentz, K. Barcus, J. Palomba, F. Paesani, S. Cohen, *Chem. Commun.* **2019**, *55*, 3481-3484.
[32] M. Katz, J. Mondloch, R. Totten, J. Park, S. Nguyen, O. Farha, J. Hupp, *Angew. Chem.* **2014**, *126*, 507-511.
[33] J. Mondloch, M. Katz, W. Isley, P. Ghosh, P. Liao, W. Bury, G. Wagner, M. Hall, J. DeCoste, G. Peterson, R. Snurr, C. Cramer, J. Hupp, O. Farha, *Nature Mater* **2015**, *14*, 512-516.
[34] A. Plonka, Q. Wang, W. Gordon, A. Balboa, D. Troya, W. Guo, C. Sharp, S. Senanayake, J. Morris, C. Hill, A. Frenkel, *J. Am. Chem. Soc.* **2017**, *139*, 599-602.
[35] Z. Zhang, C.-A. Tao, J. Zhao, F. Wang, J. Huang, J. Wang, *Catalysts* **2020**, *10*, 1086-1098.
[36] G. Zhu, S. Feng, J. Chao, W. Zheng, C. Shao, *Ceram. Inter.* **2020**, *46*, 2530-2537.
[37] Y. Wang, M. Peñas-Garzón, J. Rodriguez, J. Bedia, C. Belver, *Chem. Eng. J.* **2022**, *446*, 137229-137241.
[38] J. Wu, X. Fang, Y. Zhu, N. Ma, W. Dai, *Energy Fuels* **2020**, *34*, 12911-12927.
[39] Z. Man, Y. Meng, X. Lin, X. Dai, L. Wang, D. Liu, *Chem. Eng. J.* **2022**, *431*, 133952.
[40] A. Crake, K. Christoforidis, A. Kafizas, S. Zafeiratos, C. Petit, *Appl. Catal. B* **2017**, *210*, 131-140.
[41] K. Nakata, A. Fujishima, *J. Photochem. Photobiol. C* **2012**, *13*, 169-189.
[42] P. Conforti, M. Braunstein, J. Dodd, *J. Phys. Chem. A* **2009**, *113*, 13752-13761.
[43] A. Emelianova, E. Basharova, A. Kolesnikov, E. Arribas, E. Ivanova, G. Gor, *J. Phys. Chem. B* **2021**, *125*, 4086-4098.
[44] M. Agrawal, D. Sava Gallis, J. Greathouse, D. Sholl, *J. Phys. Chem. C* **2018**, *122*, 26061-26069.
[45] M. Grandcolas, T. Cottineau, A. Louvet, N. Keller, V. Keller, *Appl. Catal B* **2013**, *138–139*, 128-140.
[46] C. Wang, X. Zhang, Y. Zhang, Y. Jia, J. Yang, P. Sun, Y. Liu, *J. Phys. Chem. C* **2011**, *115*, 22276-22285.
[47] V. Štengl, T. Grygar, *Inter. J. Photoenergy* **2011**, *2011*, 1-13.
[48] B. Ohtani, O. Prieto-Mahaney, D. Li, R. Abe, *J. Photochem. Photobiol. A* **2010**, *216*, 179-182.
[49] S. Cai, W. Li, P. Xu, X. Xia, H. Yu, S. Zhang, X. Li, *Analyst* **2019**, *144*, 3729-3735.
[50] D. Sun, W. Liu, M. Qiu, Y. Zhang, Z. Li, *Chem. Commun.* **2015**, *51*, 2056-2059.
[51] A. Wang, Y. Zhou, Z. Wang, M. Chen, L. Sun, X. Liu, *RSC Adv.* **2016**, *6*, 3671-3679.
[52] G. Decker, Z. Stillman, L. Attia, C. Fromen, E. Bloch, *Chem. Mater.* **2019**, *31*, 4831-4839.
[53] R. Li, W. Zhang, K. Zhou, *Adv. Mater.* **2018**, *35*, 1705512.
[54] H. JiaHui, L. Xuefang, S. Jinsheng, Y. Shuguang, Z. YuCui, W. Hao, R. Chunyan, *Int. J. Hydrogen Energy* **2020**, *45*, 2852-2861.
[55] Y. Yang, K. Ye, D. Cao, P. Gao, M. Qiu, L. Liu, P. Yang, *ACS Appl. Mater. Interfaces* **2018**, *23*, 19633-19638.
[56] D. Pallotti, L. Passoni, P. Maddalena, F. Di Fonzo, S. Lettieri, *J. Phys. Chem. C* **2017**, *121*, 9011-9021.
[57] O. Carp, *Prog. Solid State Chem.* **2004**, *32*, 33-177.
[58] J. Yu, J. Lin, D. Lo, S. K. Lam, *Langmuir* **2000**, *16*, 7304-7308.
[59] J. Porter, Y. Li, C. Chan, *J. Mater. Sci.* **1999**, *34*, 1523-1531.
[60] N. Takeda, N. Iwata, T. Torimoto, H. Yoneyama, *J. Catal.* **1998**, *177*, 240-246.
[61] J. Holtzclaw, J. Wyatt, J. Campana, *Org. Mass Spectrom.* **1985**, *20*, 90-97.

[62] S. Mukhopadhyay, M. Schoenitz, E. Dreizin, *Defence Technol.* **2021**, *17*, 1095-1114.
[63] D. Chen, J. Ratliff, X. Hu, W. Gordon, S. Senanayake, D. Mullins, *Surf. Sci.* **2010**, *604*, 574-587.

Supplementary Informations

Fig.S1: Tubular Pyrex reactor coated with 200 mg of photocatalyst

Prior to the coating, the Pyrex reactor was placed in an oven preheated at 100°C during 12 h. 200 mg of photocatalyst were introduced into 20 mL of ethanol, and sonicated during 45 min. The ethanolic slurry was stirred for 1 h. The Pyrex reactor was placed on a horizontal uniaxial rotator to assure the constant rotation of the reactor during the coating process. Coating of the Pyrex reactor was performed by pipetting the photocatalyst ethanolic slurry and homogeneous deposit it onto the inner diameter of the Pyrex reactor. The photocatalyst coated reactor was finally heated locally via a heat gun until the total evaporation of ethanol, and dried in an oven preheated at 100 °C during 24 h, obtaining a surface coverage of 0,66 $mg.cm^{-2}$ for all the materials investigated.

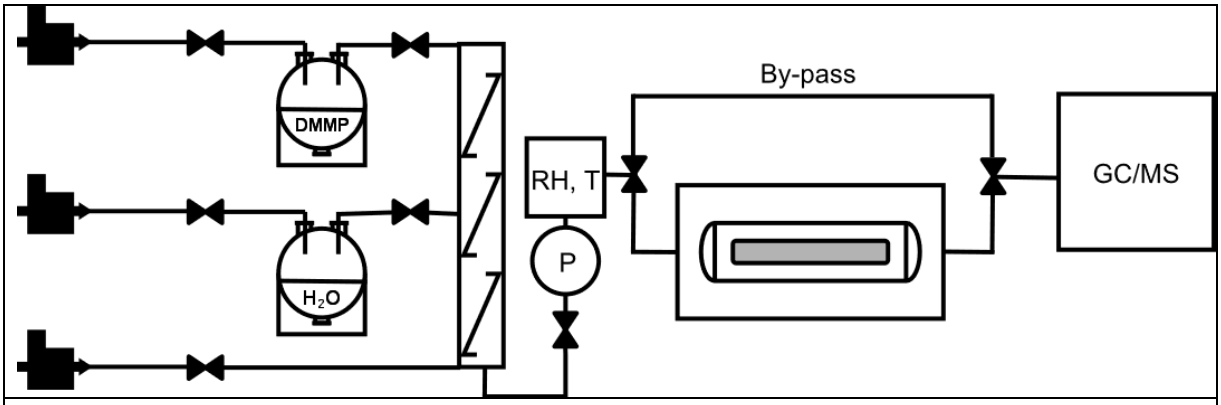

Fig.S2: Photocatalytic assessment set-up, with pressure detectors (P), relative humidity (RH) and temperature (T) controllers

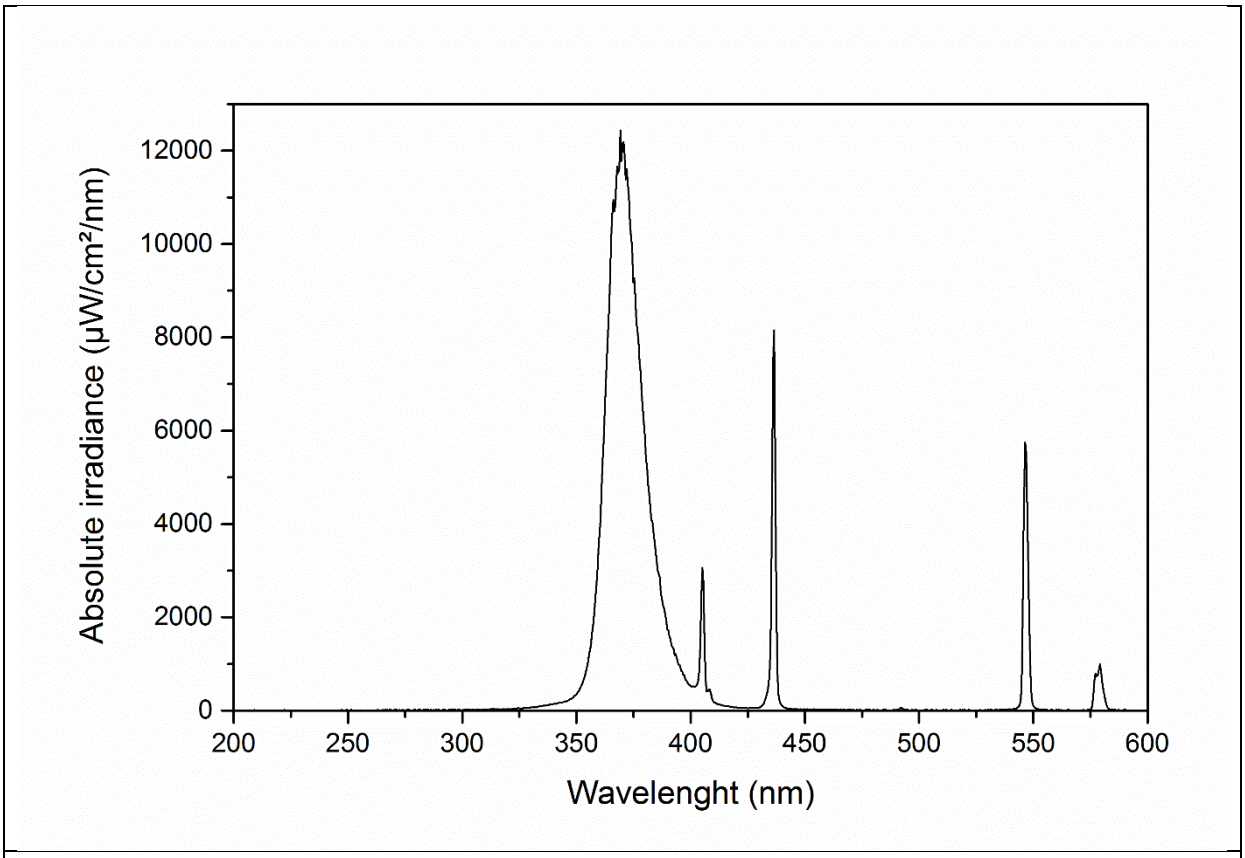

Fig.S3: Irradiance spectrum of Sylvania F8W T5 BL368 tubular lamp over the 200 to 600 nm range at a distance of 2 cm, measured by an Ocean Optics STS Microspectrometer CMOS

Table S1: Crystallite thickness of references TiO_2, UiO-66 and of UiO-66/TiO_2 composites calculated from Debye-Scherrer equation.

Sample	TiO_2 anatase crystallite thickness (nm)	TiO_2 rutile crystallite thickness (nm)	UiO-66 crystallite thickness (nm)
UiO-66	-	-	21 ± 2
Annealed UiO-66	-	-	38 ± 2
P25	21 ± 2	33 ± 2	-
Annealed P25	20 ± 2	30 ± 2	-
NS	9 ± 2	-	-
Annealed NS	9 ± 2	-	-
10wt% UiO-66/P25	19 ± 2	29 ± 2	31 ± 2
15wt% UiO-66/P25	19 ± 2	28 ± 2	26 ± 2
30wt% UiO-66/P25	20 ± 2	30 ± 2	35 ± 2
10wt% UiO-66/NS	9 ± 2	-	45 ± 2
15wt% UiO-66/NS	9 ± 2	-	48 ± 2
30wt% UiO-66/NS	9 ± 2	-	38 ± 2

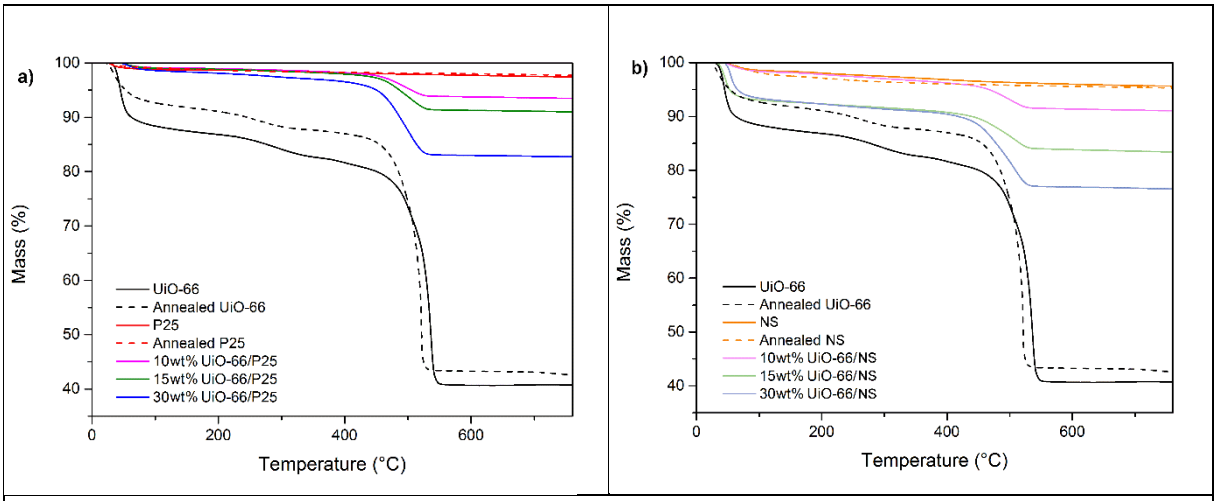

Fig.S4: TGA analysis of (a) UiO-66/P25 and (b) UiO-66/NS composites, compared to bare and annealed TiO_2 and UiO-66 counterparts.

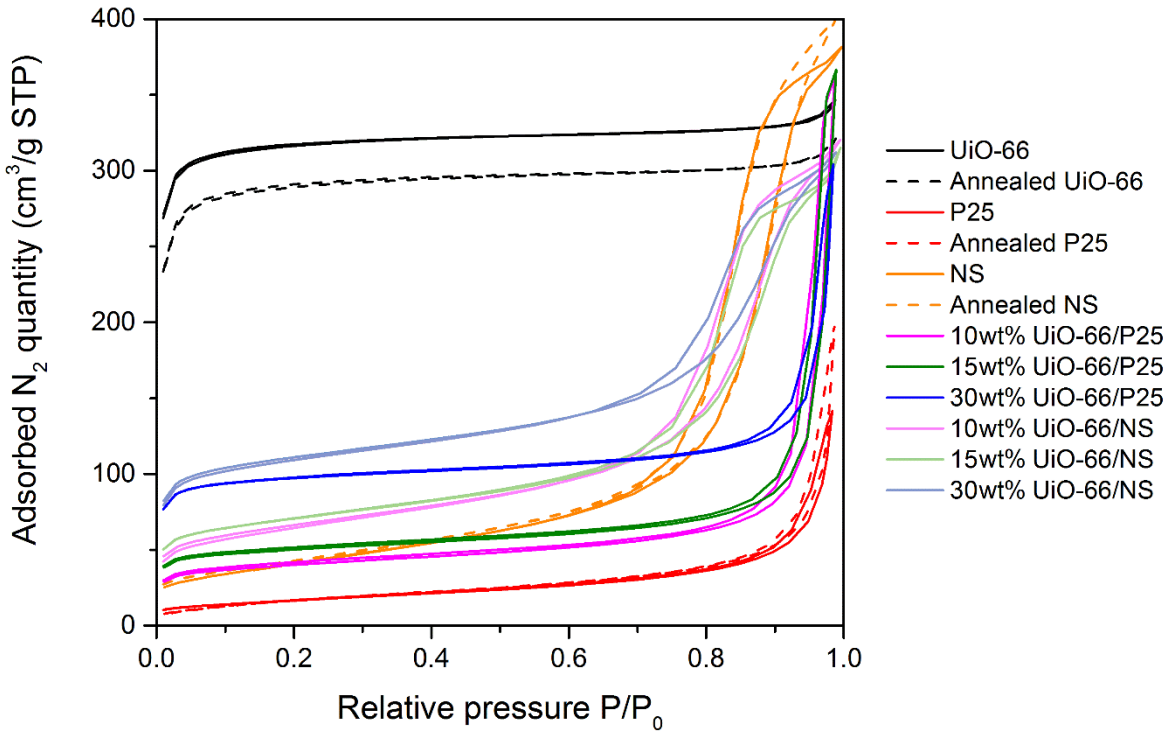

Fig.S5: BET analysis of adsorption-desorption isotherms of UiO-66/TiO_2 composites compared to bare and annealed TiO_2 and UiO-66 counterparts.

BET surface areas calculated from N_2 adsorption-desorption isotherms (Fig S4.) present UiO-66 as a microporous material with a type I isotherm, according to IUPAC classification. P25 and NS are mesoporous materials, with type V isotherm for the former, and type IV isotherm for the latter. Both present adsorption hysteresis. P25 hysteresis is of type H3 and ascribes slit-shaped pores of size centered around 2 nm. NS hysteresis is of type H2, suggesting a disordered material with bottleneck constrictions, with pore size of *ca* 13 nm. UiO-66 exhibits high surface area of *ca* 1022 m^2/g and P25 of *ca* 64 m^2/g. UiO-66/P25 and UiO-66/NS composites present type IV isotherm, keeping the type of hysteresis of their TiO_2 counterpart.

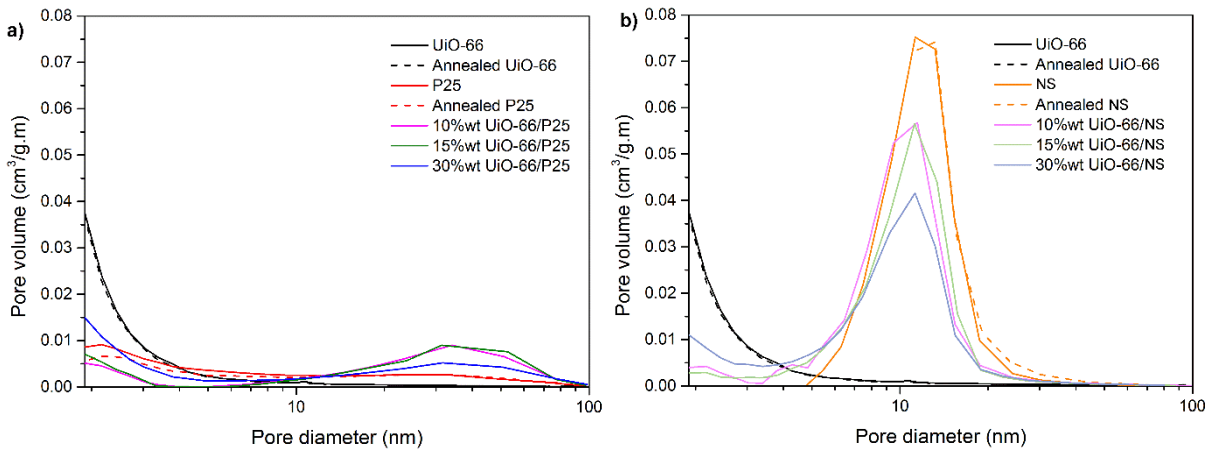

Fig.S6: Pores distribution of (a) UiO-66/P25 composites and (b) UiO-66/composites, compared to bare and

annealed TiO_2 and UiO-66 counterparts.

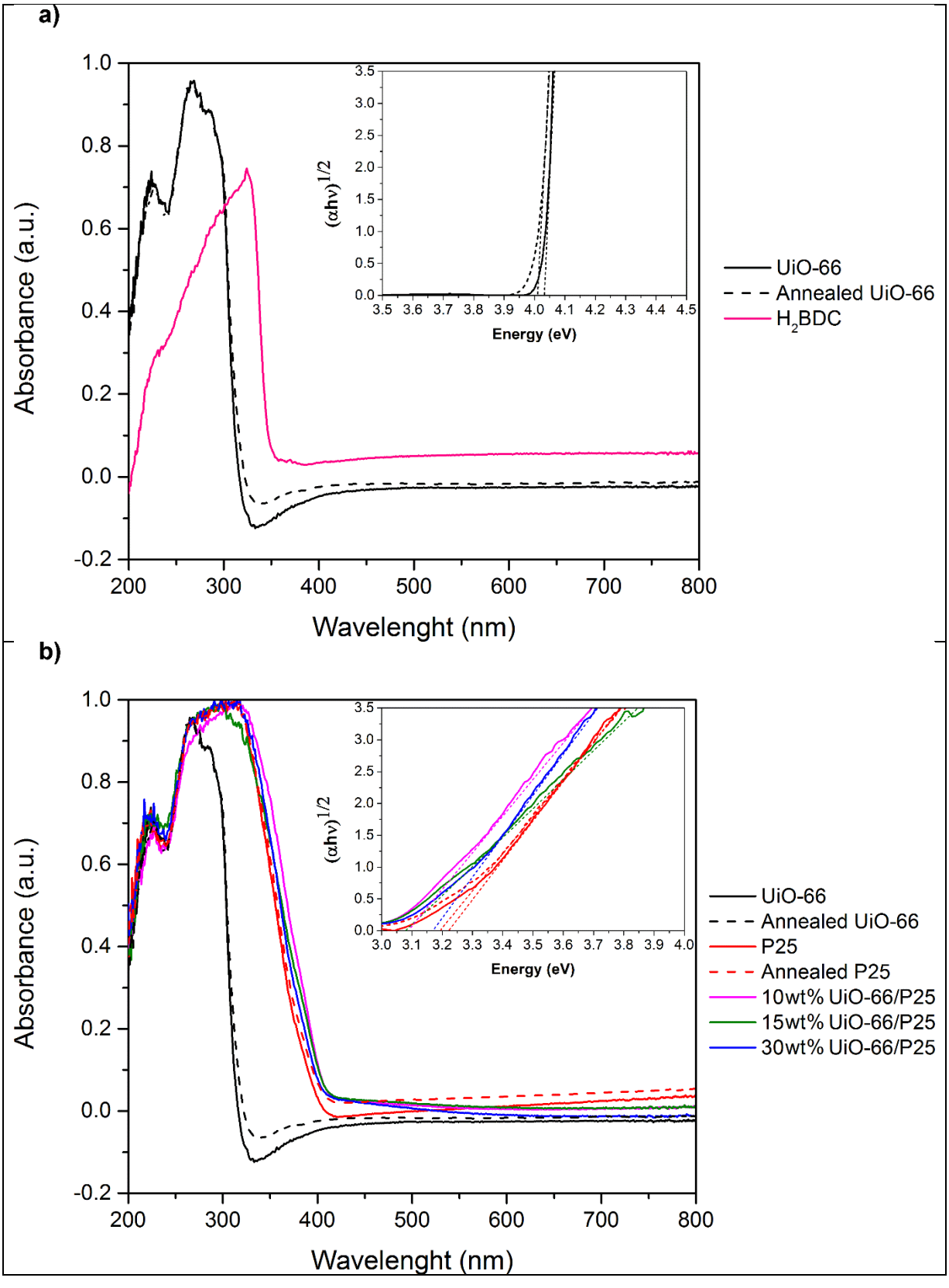

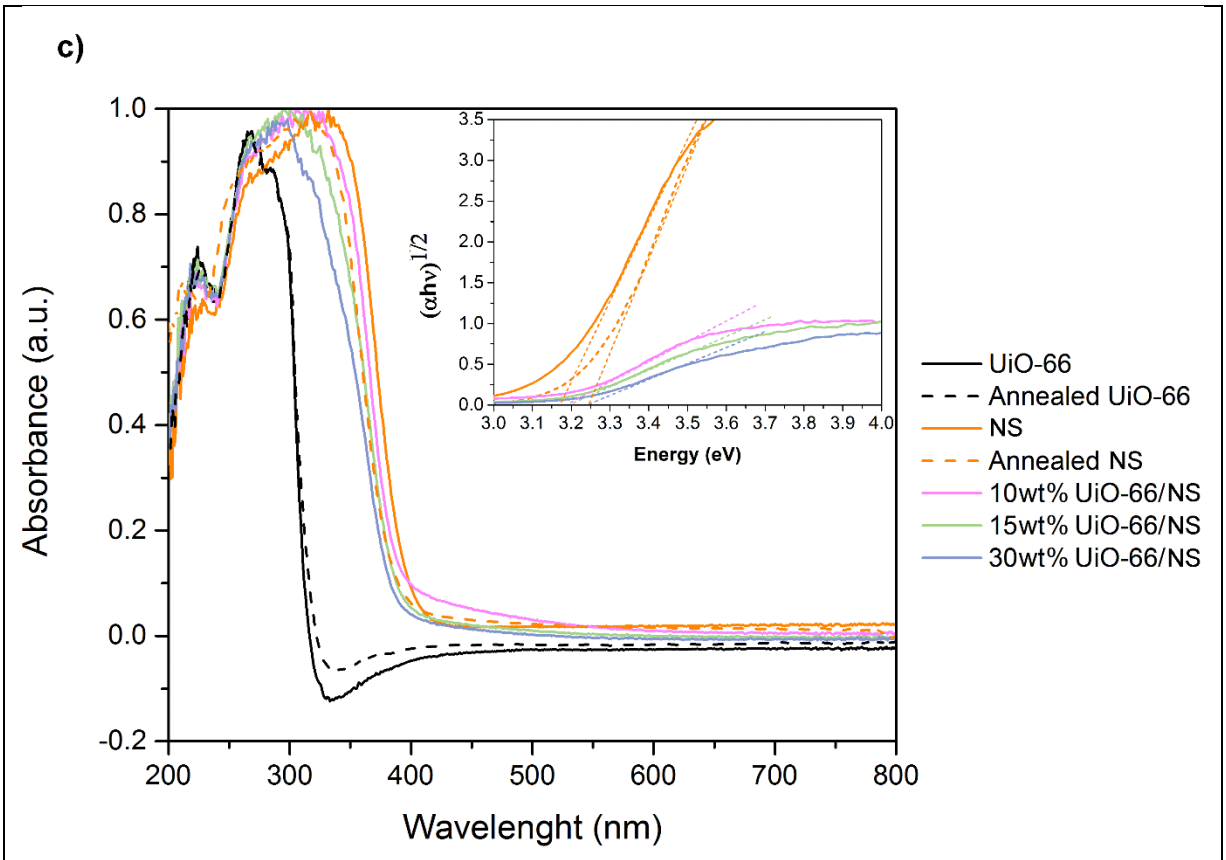

Fig.S7: UV-Visible absorbance and Tauc plot of: (a) UiO-66 and H_2BDC, (b) UiO-66/P25 and (c) UiO-66/NS composites, compared to bare and annealed TiO_2 and UiO-66 counterparts.

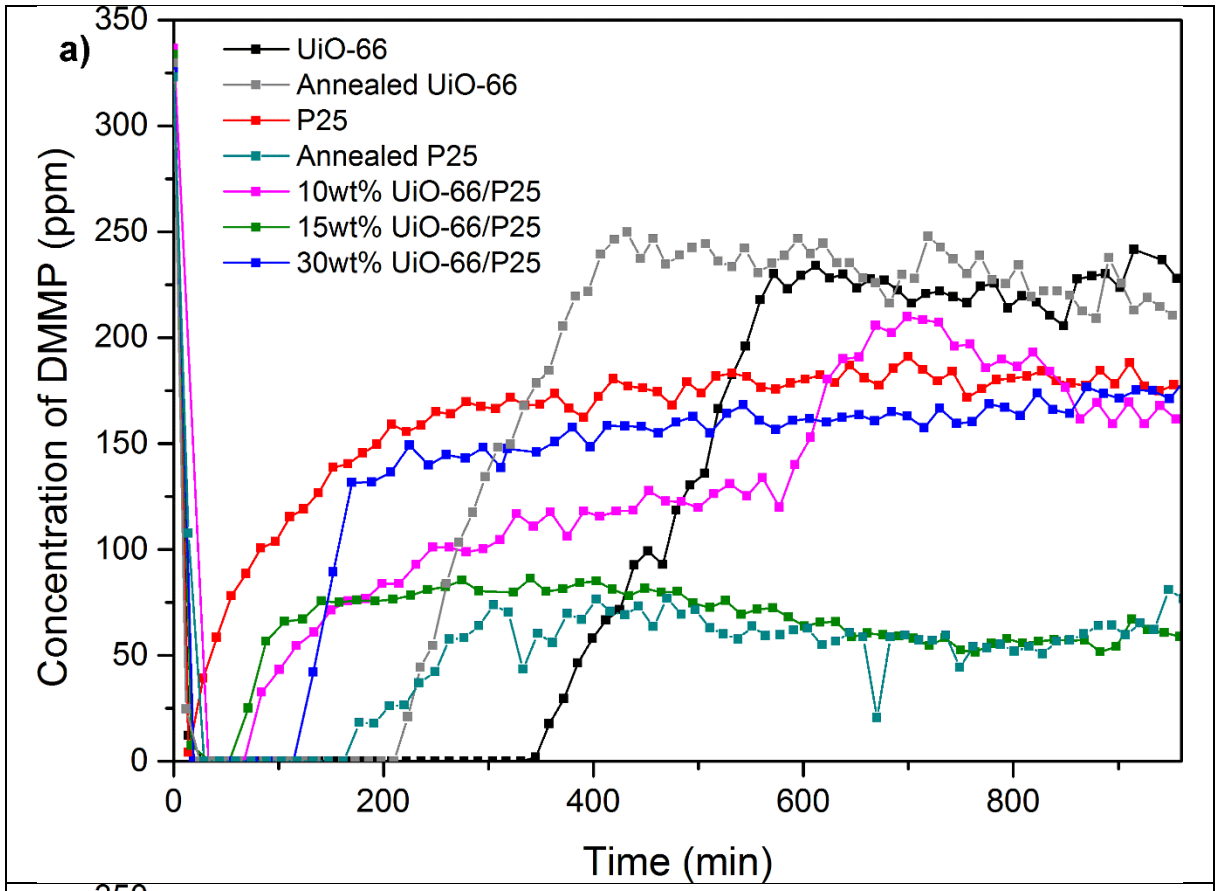
a)
UiO-66
Annealed UiO-66
P25
Annealed P25
10wt% UiO-66/P25
15wt% UiO-66/P25
30wt% UiO-66/P25
Concentration of DMMP (ppm)
Time (min)
0
50
100
150
200
250
300
350
0
200
400
600
800

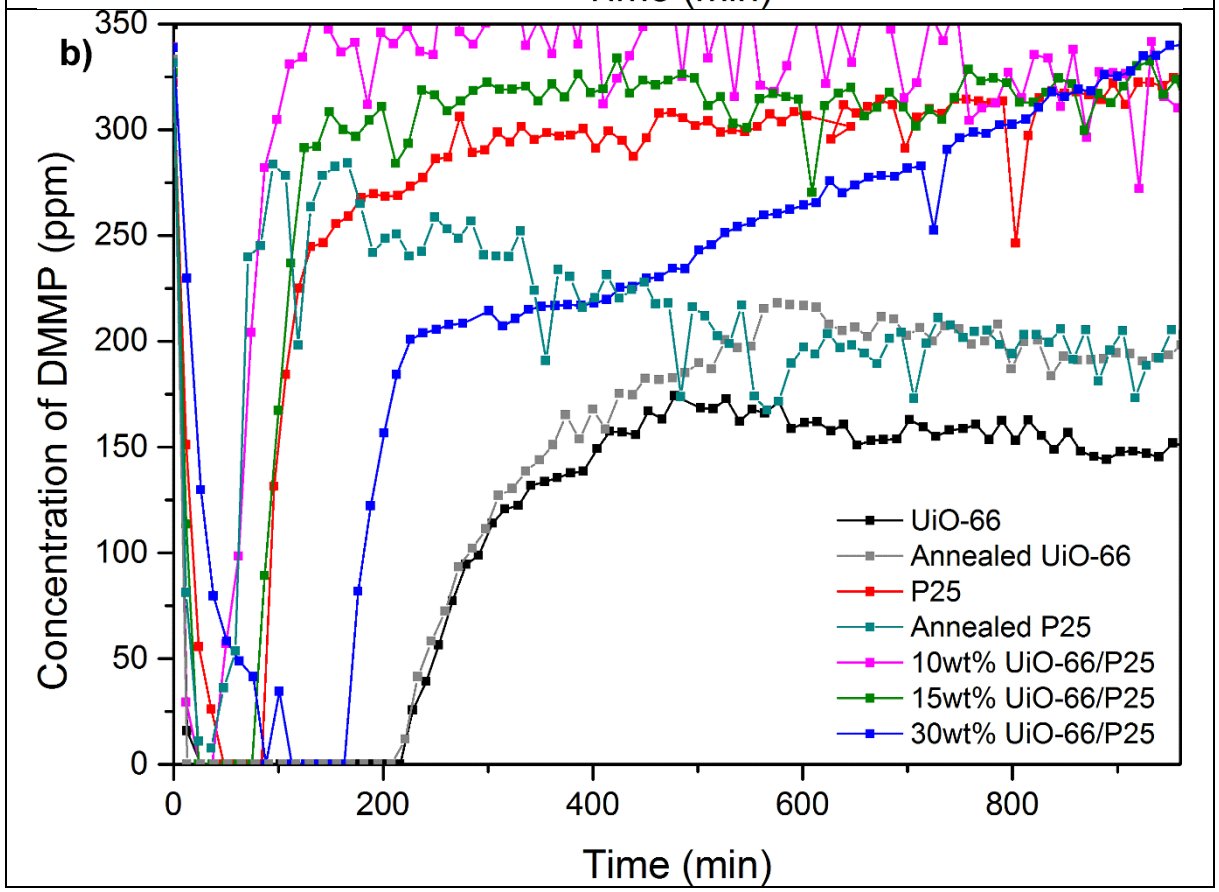
b)
UiO-66
Annealed UiO-66
P25
Annealed P25
10wt% UiO-66/P25
15wt% UiO-66/P25
30wt% UiO-66/P25
Concentration of DMMP (ppm)
Time (min)
0
50
100
150
200
250
300
350
0
200
400
600
800

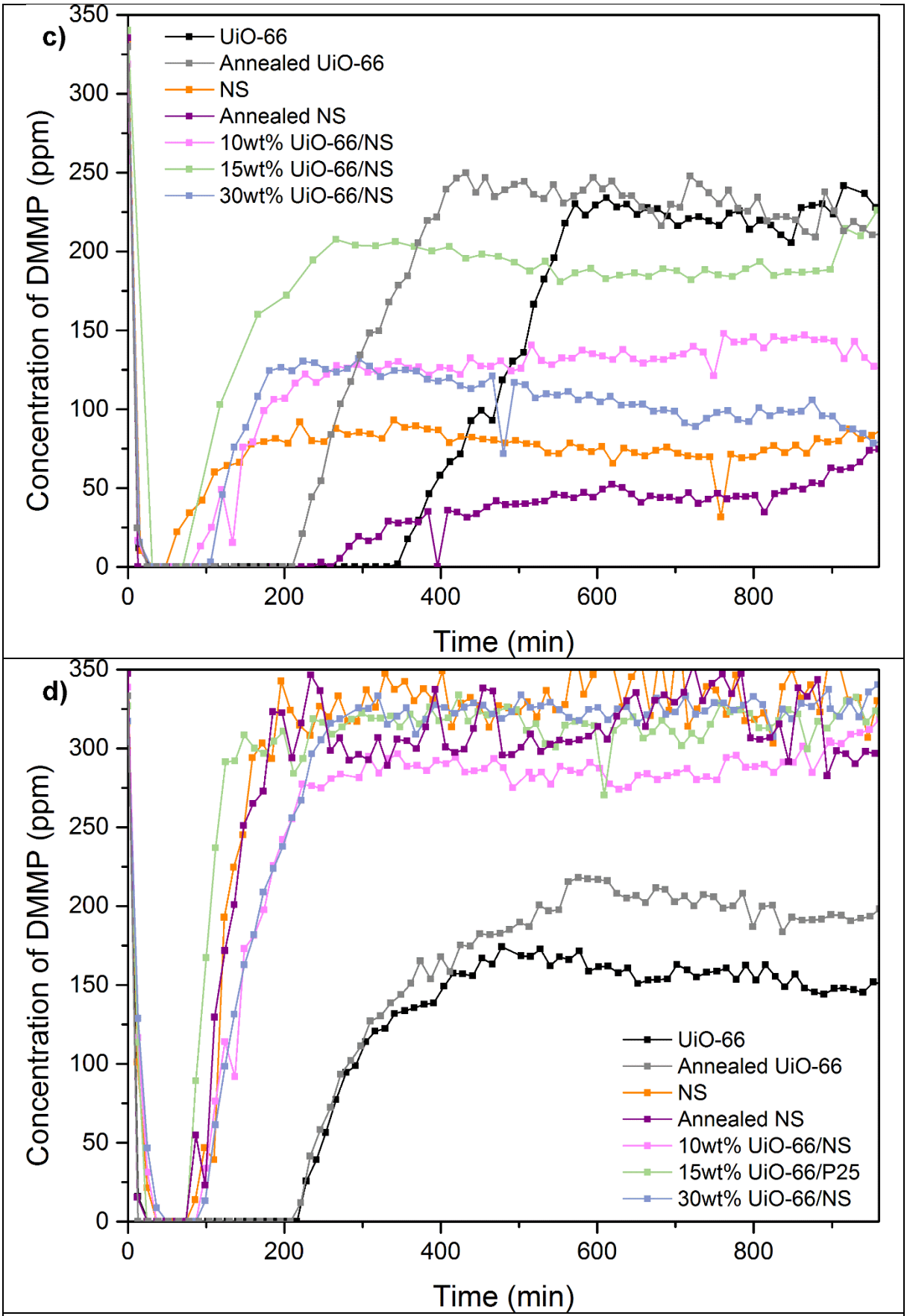

Fig.S8: DMMP photocatalytic abatement curves of: (a) UiO-66/P25 composites under UV, (b) UiO-66/P25 composites in the dark, (c) UiO-66/NS composites under UV and (d) UiO-66/NS composites in the dark, compared to bare and annealed TiO_2 and UiO-66 counterparts.

For abatement tests performed with the UV photoexcitation, the UV-A lamp was switched on at the same time than the DMMP-laden flow introduced in the reactor, adsorption and photodecontamination occurred simultaneously, described by a strong decrease of the DMMP concentration. For all samples except bare P25, total DMMP decontamination was reached. The duration of this total DMMP elimination is called the breakthrough time. This total elimination was followed by an increase in DMMP concentration, probably due to partial saturation/poisoning of adsorption sites, followed by mid-term stabilization. In addition to the duration of total DMMP elimination, those stabilized properties can also be considered as a relevant indicator to show and to compare the real photocatalytic properties of all the materials, even for UiO-66 that can exhibit photocatalytic activity.

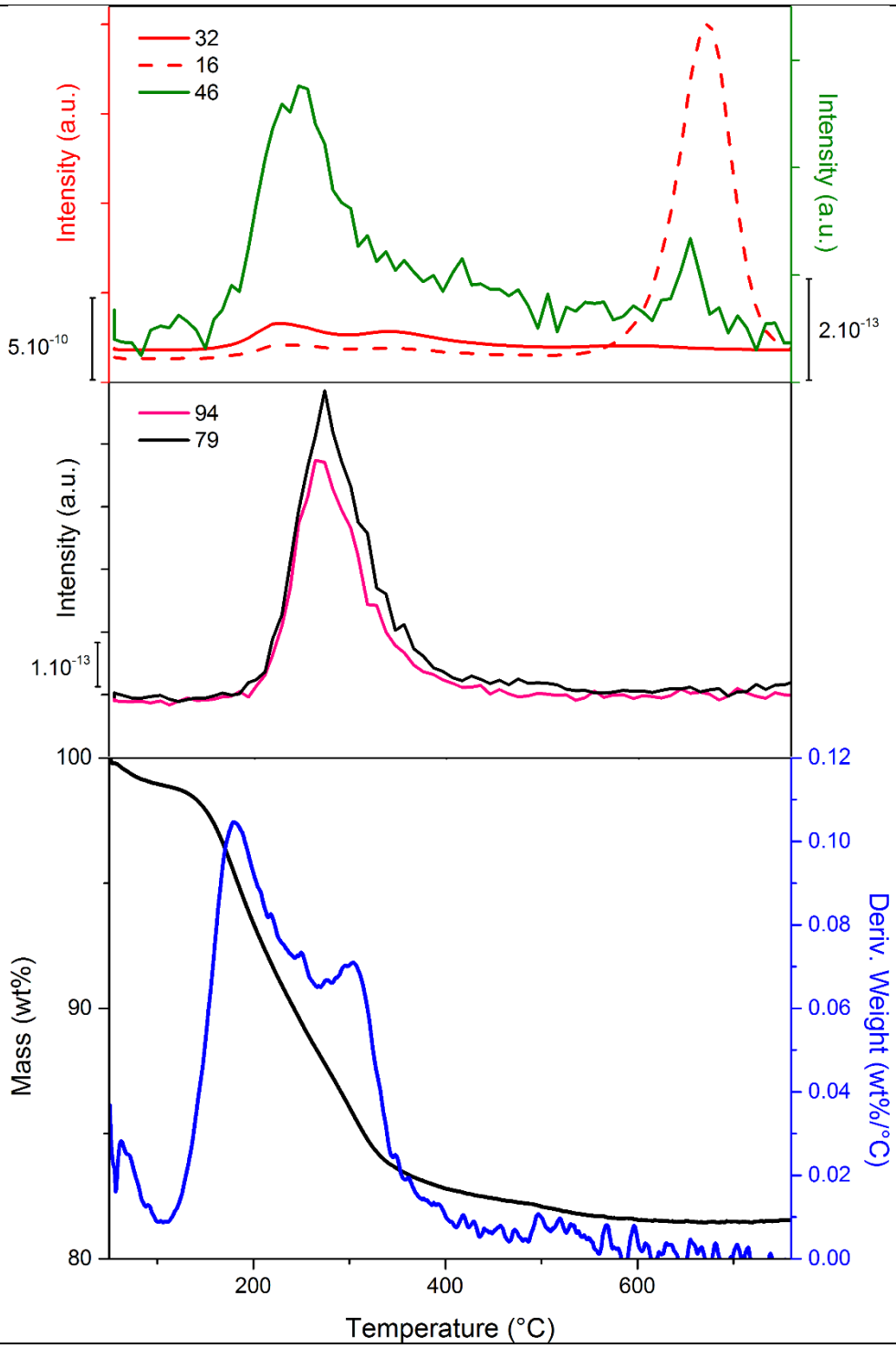

Fig.S9: TPD/MS coupled to TGA analysis of 10 wt% UiO-66/P25 before and after DMMP-decontamination.

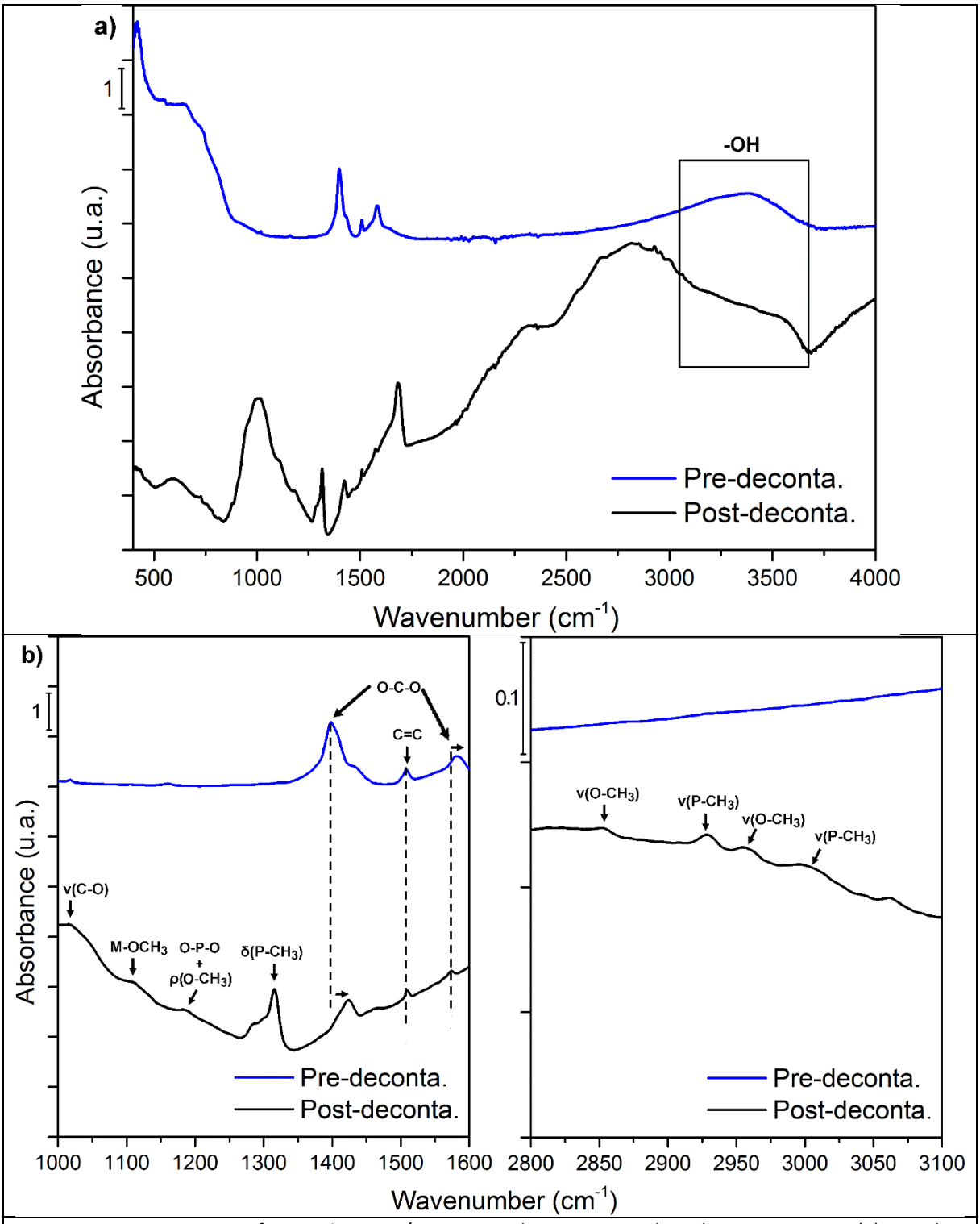

Fig.S10: ATR-FTIR spectra of 10 wt% UiO-66/P25 pre- and post-DMMP-photodecontamination: (a) complete spectra from 400 to 4000 cm^{-1}, and (b) highlight on P-O bonds [1-6]

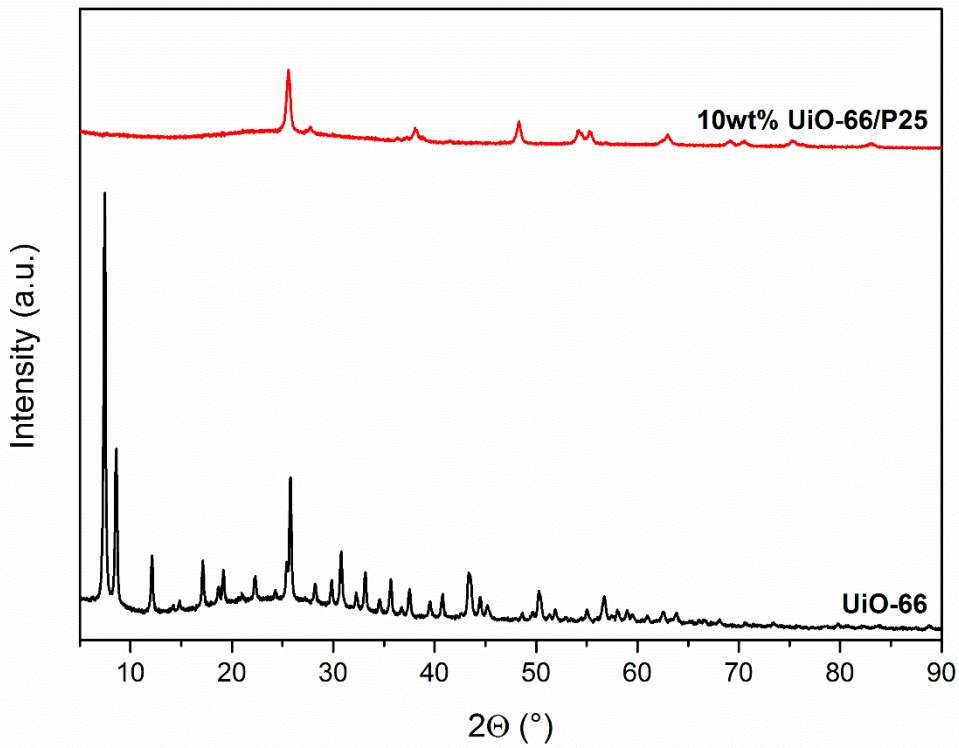

Fig.S11: XRD pattern of UiO-66 and 10 wt% UiO-66/P25 post-DMMP-photodecontamination

References.

[1] C. Rusu, J. Yates, *J. Phys. Chem. B*, **2000**, *104*, 12292-12298

[2] S. Mukhopadhyay, M. Schoenitz, E. Dreizin, *Defence Technol.* **2021**, *17*, 1095-1114.

[3] J. Hafizovic Cavka, S. Jakobsen, U. Olsbye, N. Guillou, C. Lamberti, S. Bordiga, K. Lillerud, *J. Am. Chem. Soc.,* **2008**, *42,* 13850-13851

[4] G. Shangkum, P. Chammingkwan, D. Trinh, T. Taniike, *Membranes*, **2018**, *8*, 129-153

[5] L. Valenzano, B. Civalleri, S. Chavan, S. Bordiga, M. Nilsen, S. Jakobsen, K. Lillerud, C. Lamberti, *Chem. Mater.,* **2011**, *23*, 1700-1718

[6] M. Kandiah, S. Usseglio, S. Svelle, U. Olsbye, K. Lillerud, M. Tilset, *J. Mater. Chem.,* **2010**, *20*, 9848-9851